universität wien

MASTERARBEIT | MASTER'S THESIS

Titel | Title

Seasonal Predator-Prey Dynamics under Varying Summer Lengths: Modeling, Classification, and Responses to Climate Change

verfasst von | submitted by

Clemens Breuß BSc

angestrebter akademischer Grad | in partial fulfilment of the requirements for the degree of

Master of Science (MSc)

Wien | Vienna, 2025

Studienkennzahl lt. Studienblatt | Degree programme code as it appears on the student record sheet:	UA 066 821
Studienrichtung lt. Studienblatt | Degree programme as it appears on the student record sheet:	Masterstudium Mathematik
Betreut von | Supervisor:	Nikolas Aksamit PhD

Abstract

This thesis presents a seasonally structured predator-prey model that captures the ecological dynamics between small rodents and mustelid predators in northern Fennoscandia. Motivated by climate-induced changes in seasonality, the model incorporates a smooth transition between summer and winter dynamics, allowing for a biologically realistic and mathematically accessible analysis of seasonal predation behavior.

A novel classification algorithm was developed to distinguish between periodic, quasiperiodic, and chaotic attractors across a wide parameter space. This enabled the construction of a detailed bifurcation diagram, revealing a rich variety of dynamical regimes and five distinct bifurcation mechanisms.

Stochastic simulations introduced seasonal variability, demonstrating that while narrow regions of distinct deterministic behavior were sensitive to noise, broader qualitative behaviors remained robust. A grid-based method was introduced to classify fuzzy attractors in noisy systems, offering a practical tool for analyzing real-world ecological data.

Finally, the study identified tipping points and asymmetries in the timescales of transitions between dynamical regimes, showing that the system can shift between ecological states at very different rates depending on the direction of change. The modeling framework and analytical tools developed in this work provide a foundation for investigating how climate-driven changes in seasonality may affect predator-prey cycles and ecosystem stability.

Keywords: predator-prey dynamics, seasonal modeling, bifurcation analysis, stochastic simulations, ecological tipping points, climate change

Zusammenfassung

Diese Arbeit entwickelt ein mathematisches Modell zur Beschreibung saisonal geprägter Räuber-Beute-Dynamiken zwischen kleinen Nagetieren und Musteliden-Räubern in Nordfennoskandinavien. Angeregt durch klimabedingte Veränderungen der Saisonalität verbindet das Modell Sommer- und Winterdynamiken über einen kontinuierlichen Übergang und ermöglicht so eine biologisch realistische und mathematisch zugängliche Analyse saisonaler Prädationsmuster.

Ein zentrales Ergebnis ist die Entwicklung eines Klassifikationsalgorithmus, der zwischen periodischem, quasiperiodischem und chaotischem Langzeitverhalten unterscheiden kann – auch bei gleichzeitig auftretenden Attraktoren. Damit konnte ein detailliertes Bifurkationsdiagramm erstellt werden, das eine Vielzahl dynamischer Regime und mehrere Bifurkationsmechanismen sichtbar macht.

Zur Berücksichtigung natürlicher Variabilität wurde das Modell um stochastische Schwankungen der Sommerlänge erweitert. Eine gitterbasierte Methode zur Klassifikation unscharfer Attraktoren wurde eingeführt und bietet ein praktisches Werkzeug zur Analyse verrauschter ökologischer Daten. Die Robustheit der übergeordneten Verhaltensmuster unter Zufallseinflüssen zeigt die strukturelle Stabilität des Modells.

Darüber hinaus wurden Kipppunkte identifiziert – Schwellenwerte, bei denen Übergänge zwischen verschiedenen Dynamiken asymmetrisch verlaufen. Das entwickelte Modellierungsframework und die analytischen Methoden bieten eine fundierte Grundlage, um die Auswirkungen klimabedingter saisonaler Veränderungen auf Räuber-Beute-Zyklen und die Stabilität von Ökosystemen zu untersuchen.

Schlagwörter: Räuber-Beute-Dynamik, saisonale Modellierung, Bifurkationsanalyse, stochastische Simulationen, ökologische Kipppunkte, Klimawandel

Acknowledgements

First and foremost, I would like to express my deepest gratitude to my supervisor, Nikolas Aksamit. I am especially thankful that he agreed to take on the unusual task of supervising a student from outside his own university. I truly appreciate the opportunity he gave me to work on such an interesting project. Throughout this journey, he granted me a great deal of freedom in choosing which directions to explore, while at the same time providing thoughtful guidance and support that kept me on track. His balance of trust and mentorship has been invaluable, and it has been a real pleasure to work with him.

I would also like to thank the responsible people at the University of Vienna, in particular Studienprogrammleiter Roland Donninger and the Büro Studienpräses, as well as all those at UiT who made this collaboration possible. Their support and willingness to enable such a cross-university project are greatly appreciated, and without their efforts this thesis could not have taken place.

Furthermore, I am very grateful to Julia Mikhailova, Nikolas Aksamit, and Nigel Yoccoz for letting me be part of the project. It gave me a first experience of collaborating with other researchers, which has been both rewarding and inspiring.

My sincere thanks also go to my friends Moritz and Kimani, who carefully read through the draft of my thesis and provided valuable feedback that greatly improved its readability.

I further acknowledge the use of AI tools, which assisted me in various aspects such as rephrasing sentences, finding synonyms, and assisting with coding and visualization. These tools helped polish the presentation of my work, while all academic decisions and conclusions remain my own.

Finally, I owe a huge thank you to all my friends and family for their incredible support throughout this process. They are truly the best I could imagine, and I want to say a heartfelt thank you, danke, tusen takk!

Inhaltsverzeichnis

1. Introduction

Population cycles, often occurring on an interannual timescale, are a well-known and widespread phenomenon in ecology and have been subject to research for a long time. Although there is still some debate about necessary and sufficient conditions for small mammal population cycles, feeding interactions between predators and prey are believed to play an important role [26]. In northern Fennoscandia specialist predators such as weasels and stoats (small mustelids) strongly influence the dynamics of small rodent populations, and thus modeling interactions between the two species can capture much of the observed population variability [17, 25]. In this thesis, we focus on the northern Fennoscandia rodent-mustelid system, where interactions between small mustelids and their rodent prey provide a rich context for studying seasonal predator-prey dynamics.

Terrestrial ecosystems in the Arctic are characterized by a strong seasonality with extended, snow-covered winters, which strongly influence population dynamics [5, 8, 23]. Seasonality and snow cover directly affect the availability of food resources for herbivores, such as small rodents, but also indirectly, as predator species can vary between the different seasons (due to migration, for example, like in birds of prey). The snow cover furthermore serves as a protective layer for small mammals, as it limits predator access to prey [18].

As such, seasonal shifts are not only a defining feature of Arctic ecosystems but also a key factor in shaping predator-prey dynamics. As climate change continues to alter the timing and duration of seasons, these shifts can disrupt established ecological interactions. In particular, altered seasonality may change predator-prey interactions, potentially increasing the risk of extinction. In northern Fennoscandia, small mustelids such as weasels and stoats act as generalists in summer but specialize on small rodents like voles and lemmings in winter - a pattern that has been well documented [17, 21]. This seasonal change in diet strongly influences prey populations by altering the intensity and selectivity of predation throughout the year. Anticipating how populations will respond to these changes is therefore essential for understanding species persistence under future climate scenarios [28, 33].

Recent ecological studies further support the need for updated models that reflect ongoing environmental changes. Ehrich et al. [10] documented population trends across Arctic sites over the past 25 years, a period marked by rapid warming. While overall small mammal abundance has not declined, notable shifts in species composition have occurred. In Fennoscandia, vole species have expanded northward, partially replacing

lemming populations - likely in response to changing climatic conditions.

Long-term observational data also suggest that the characteristic population cycles of small mammals may be weakening. Henden et al. [19] analyzed historical fox bounty records and found that while strong cycles were once prevalent in northern regions, they have become less pronounced in recent decades. This shift may reflect a broader transition from regular cycles to more irregular or chaotic dynamics, potentially driven by climate-induced changes in seasonality and predator-prey interactions.

Combining this change in predation behavior with changing climate and environmental conditions - especially shorter and warmer winters [30] - it is of great interest to investigate possible changes in population dynamics.

Several models have been have been proposed to recreate seasonal influences on small rodent and mustelid dynamics. In a pioneering paper, Hanski et al. (summary in [20]) modeled the impact of seasonality by varying death and reproduction parameter values between winter and summer. This approach demonstrated that even relatively simple seasonal switching can produce complex dynamics, including multi-year limit cycles and chaotic behavior [17, 41].

Building on this foundation, Tyson and Lutscher [42] proposed a more flexible framework by introducing separate equations for summer and winter dynamics. This allows for qualitatively different predator-prey interactions across seasons, such as a shift from generalist to specialist predation. While their model was developed for a different predator-prey system (owls and snowshoe hares in Canada), the underlying mechanism applies to a broad range of seasonally influenced predator-prey systems, and in particular, the rodent-mustelid system.

In this thesis, I aim to answer the following question: *How do changes in seasonal transitions affect the dynamics of small rodent populations in northern Fennoscandia?* With this goal in mind, the proposed research addressed the following five objectives:

1. **Develop the simplest possible seasonal predator-prey model** that captures the essential dynamics between small rodents and mustelids under a two-season framework. The model is parameterized to reflect the dynamics of these species, ensuring realistic behavior while retaining generality for other seasonally driven predator-prey systems. To build the model, we define separate equations for summer and winter dynamics, incorporating the empirically observed seasonal switch in predation behavior. Model parameters are initially set based on literature values and expert knowledge, allowing the simplest possible formulation that can still reproduce observed population patterns.

2. **Introduce a classification algorithm** to identify all long-term behaviors in simulation data, including limit cycles, quasiperiodicity, and chaotic dynamics. This algorithm systematically analyzes population time series from simulations,

allowing us to determine all possible stable and complex dynamics for a given parameter set. The method builds on previous approaches to classify multi-year cycles and chaotic dynamics in predator-prey systems.

3. **Construct bifurcation diagrams and test robustness under parameter uncertainty** by varying summer length and one intrinsic model parameter. Because these models contain many parameters, and some are difficult to observe in the field, this objective explicitly focuses on *parameter uncertainty and robustness*. In particular, we identify the most uncertain parameter and investigate how climate-driven changes in summer length affect dynamics across a plausible range of other parameters. By simulating the model over a two-dimensional grid of these parameters, we map regions of qualitatively distinct long-term behaviors and assess the structural stability of the system under different scenarios.

4. **Simulate stochastic changes in summer length** to examine the system's response to realistic environmental variability. Small yearly fluctuations are introduced into the model, and the resulting dynamics are analyzed to assess structural stability across the bifurcation diagram.

5. **Analyze transitions across bifurcation boundaries** to study how the system responds when moving from one dynamic regime to another. We examine the speed of convergence to new attractors and investigate whether there is any directional mismatch in crossing boundaries, which may indicate hysteresis or sensitive dependence on the direction of parameter change.

The code for all simulations was written in *Python* and is available in a private *GitHub* repository accessible via *GitFront*: `https://gitfront.io/r/clebreuss/Z86dHpkXnGxM/predator-prey-seasonality/`. It includes foundational routines developed collaboratively in a previous project (see [32]) as well as additional code written specifically for this Master's thesis.

2. Methods and theoretical groundwork

In this section, we define and describe the methods that are necessary to investigate the behavior of our predator-prey system mathematically. We keep the definitions rather general, but still have our ecological system of interest always in mind.

2.1. Poincaré sections and Poincaré maps

Proposition 2.1.1. *[43] An n-dimensional non-autonomous system of ordinary differential equations,*

$$\frac{d\mathbf{x}}{dt} = f(\mathbf{x}, t), \quad \mathbf{x} \in \mathbb{R}^n$$

can be embedded in an $n+1$-dimensional autonomous system of ODE's by introducing an additional variable $\tau := t$:

$$\begin{aligned} \frac{d\mathbf{x}}{dt} &= f(\mathbf{x}, \tau), \\ \frac{d\tau}{dt} &= 1. \end{aligned}$$

For our predator-prey system, $n = 2$, and the embedding gives a three-dimensional autonomous system. Motivated by the strong impact of seasonality (i.e. switching winter- and summer-predation behavior), this extension from a two-dimensional system to a third dimension reflects the importance of time dependence of the differential equations. However, since the seasonal forcing is periodic, the system is not truly defined on $\mathbb{R}^3$, but rather on $\mathbb{R}^2 \times S^1$, where the circle S^1 represents the annual cycle of time. This perspective allows us to study the year-to-year dynamics using Poincaré maps.

Definition 2.1.1. *[2] Consider the system*

$$\frac{d\mathbf{x}}{dt} = f(\mathbf{x}, t), \quad \mathbf{x} \in \mathbb{R}^n,$$

suppose that f is sufficiently smooth on some subset of $\mathbb{R}^n$ and let φ denote the flow generated by our system. Suppose that there exists a $n-1$ dimensional surface Σ such

that the orbits in our system consistently return to Σ, but are never tangent to it. That means, for $\mathbf{x}_0 \in \Sigma$, $\varphi(\mathbf{x}_0, \tau(\mathbf{x}_0)) \in \Sigma$ after some time $\tau(\mathbf{x}_0) > 0$. The map that associates points on Σ with their points of first return to Σ is called ***Poincaré map****, and we denote it by P.*

$$\begin{aligned} P: \quad & \Sigma \to \Sigma \\ & \mathbf{x_0} \mapsto \varphi(\mathbf{x}_0, \tau(\mathbf{x}_0)) \end{aligned}$$

The surface Σ is called ***Poincaré section****.*

We can use this definition to introduce a Poincaré section tailored to the seasonal structure of our system.

Proposition 2.1.2. *[9] Let $\frac{d\mathbf{x}}{dt} = f(\mathbf{x}, t)$ with $\mathbf{x} \in \mathbb{R}^2$ and assume f to be periodic with period T, i.e. $f(\mathbf{x}, t_0) = f(\mathbf{x}, t_0 + T)$.*

Then, the Poincaré section

$$\Sigma = \{(\mathbf{x}, \tau) \in \mathbb{R}^2 \times \mathbb{R} | \tau \equiv \tau_0 \, (mod\, T)\}$$

is defined for some fixed $\tau_0 \in [0, T)$.

Furthermore, since the flow is autonomous in the extended space, we can introduce the ***stroboscopic Poincaré map***

$$P : \mathbb{R}^2 \to \mathbb{R}^2, \quad P(\mathbf{x}_0) = \mathbf{x}(\tau_0 + T),$$

where $\mathbf{x}(\tau)$ is the solution for $\mathbf{x}(\tau_0) = \mathbf{x}_0$.

Keeping this notion, we see that we can use the Poincaré map to determine whether the solution trajectories are periodic.

Proposition 2.1.3. *If f is periodic with period $T = 1$ and $P(\mathbf{x}) = \mathbf{x}$, then $\mathbf{x}$ is a fixed point of the Poincaré map, i.e. $\mathbf{x}$ lies on a periodic orbit of period 1.*

Furthermore, if there exists a $k \in \mathbb{N}$ such that $P^k(\mathbf{x}) = \mathbf{x}$ (i.e. $\mathbf{x}$ is a fixed point of the iterated map P^k) and k is the smallest such number, then $\mathbf{x}$ lies on a periodic orbit of period k.

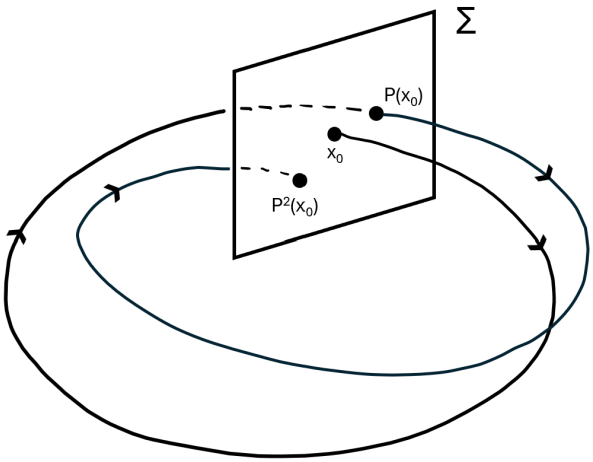

Figure 2.1.: Poincaré map and Poincaré section.

2.2. Jacobian and stability of cycles

To obtain the stability of periodic solution trajectories, it is sufficient to look at the Jacobian of the Poincaré map. First, we focus on the case of a fixed point $\mathbf{x}$ of the Poincaré map, so at a periodic orbit of period 1.

Definition 2.2.1 (Closed Orbit Stability Criterion)**.** *[2] Let $DP(\tilde{\mathbf{x}})$ be the Jacobian of the Poincaré map P evaluated at a fixed point $\tilde{\mathbf{x}}$. Furthermore let λ_1 and λ_2 be the eigenvalues of $DP(\tilde{\mathbf{x}})$. Then the closed orbit corresponding to $\tilde{\mathbf{x}}$ is stable if and only if $|\lambda_i| < 1$ for all i.*

Remark 2.2.1. This definition holds not only for two dimensions, but also in general for an n-dimensional system.

Now assume that we have a k-periodic orbit with $P^k(\mathbf{x}_1) = \mathbf{x}_1$. More precisely, denote the points on the Poincaré map that are visited before returning to $\mathbf{x}_1$ by $\mathbf{x}_2, \dots \mathbf{x}_k$. We can write this as $P(\mathbf{x}_i) = \mathbf{x}_{i+1}$ for $i \in \{1, \dots, k-1\}$ and $P(\mathbf{x}_k) = \mathbf{x}_1$.

We use this notation to generalize the definition for stability to a k-periodic orbit as follows.

Definition 2.2.2 (Stability of k-cycles)**.** *[3] Let $\{\mathbf{x}_1, \dots, \mathbf{x}_k\}$ denote the subsequent points on the Poincaré section of a k-periodic orbit starting at $\mathbf{x}_1$. Then, this orbit is*

stable if and only if the eigenvalues λ_1 and λ_2 of the Jacobian of the k-iterated Poincaré map fulfill $|\lambda_i| < 1$ for all $i \in \{1, 2\}$. This Jacobian is given by

$$\begin{aligned} DP^k(\mathbf{x}_1) &= D(P^{k-1}(P(\mathbf{x}_1)) = DP^{k-1}(P(\mathbf{x}_1))DP(\mathbf{x}_1) = DP^{k-1}(\mathbf{x}_2)DP(\mathbf{x}_1) \\ &= \cdots = DP(\mathbf{x}_k)\cdots DP(\mathbf{x}_1). \end{aligned}$$

Remark 2.2.2. Definition 2.2.2 implies that it does not matter for which of the k points along the k-cycle the stability is calculated. The Jacobian of the k-times iterated map evaluated at each of these points is the same.

Remark 2.2.3. The formula for the Jacobian in Definition 2.2.2 simply stems from applying the chain rule to the iterated map P, i.e.

$$(f \circ g(x))' = f'(g(x))g'(x).$$

When one cannot solve the system of equations analytically (for example if one has a highly complicated, nonlinear right-hand side f), but only numerically, the Jacobian can also not be explicitly calculated. However, the Jacobian can be approximated by the method of finite differences.

Proposition 2.2.1. *[30] Let $J = DP(\mathbf{x})$ be the Jacobian of the Poincaré map evaluated at a point $\mathbf{x}$. Then, J can be approximated by the central finite-difference approximation*

$$J_{ij} \approx \frac{P_i(\mathbf{x} + h\mathbf{e}_j) - P_i(\mathbf{x} - h\mathbf{e}_j)}{2h},$$

where P_i denotes the i-th component of the solution $\mathbf{y} = P(\mathbf{x})$ of the Poincaré map computed at $\mathbf{x}$, $\mathbf{e}_j$ the jth unit vector and $h << 1$.

Remark 2.2.4. The finite-difference approximation to the Jacobian holds only for one iteration of the Poincaré map. To approximate the stability of a periodic orbit of period $k > 1$, one can however just proceed as in Definition 2.2.2 and calculate the approximations for one iteration of the map, starting at all the intermediate points belonging to the k-cycle separately and perform matrix multiplication afterwards.

2.3. Finite-Time Lyapunov Exponents (FTLE)

To get some notion of stability of non-fixed or non-periodic points of a (Poincaré-) map, the concept of Lyapunov exponents is quite handy. We ask the following question. If two trajectories start very close together, do they remain close, or do they diverge (rapidly) as time progresses? The Lyapunov exponent provides a quantitative answer

to this question - it measures the average exponential rate at which nearby trajectories separate (or converge) under the flow of the system. This following section is based on [2].

To formalize the idea, we consider a small perturbation $\varepsilon\mathbf{e_0}$ with $\|\mathbf{e_0}\| = 1$ to an initial condition $\mathbf{x_0}$, and study how this perturbation evolves under the linearized dynamics. The Lyapunov exponent captures the long-term behavior of the norm of this deviation vector, normalized by its initial size.

Definition 2.3.1 (Lyapunov Exponent)**.** *[2] Let $\varphi(\mathbf{x_0}, t)$ be the flow map of a smooth dynamical system defined by*

$$\frac{d}{dt}\mathbf{x}(t) = f(\mathbf{x}(t)), \quad \mathbf{x}(0) = \mathbf{x_0},$$

*and let $D\varphi(\mathbf{x_0}, t)$ denote the Jacobian of the flow with respect to the initial condition $\mathbf{x_0}$. For a small perturbation $\varepsilon\mathbf{e_0}$ for $\|\mathbf{e_0}\| = 1$ and $\varepsilon > 0$, the **Lyapunov exponent** in the direction of $\epsilon\mathbf{e_0}$ is defined as*

$$\lambda(\mathbf{x_0}, \varepsilon\mathbf{e_0}) = \lim_{t\to\infty} \frac{1}{t} \ln\left(\frac{\|D\varphi(\mathbf{x_0}, t)\varepsilon\mathbf{e_0}\|}{\|\varepsilon\mathbf{e_0}\|}\right),$$

if the limit exists.

Remark 2.3.1. The name *exponent* reflects the fact that, for small perturbations $\epsilon\mathbf{e_0}$, the linearized dynamics suggest that the deviation at time t behaves approximately like

$$\|D\varphi(\mathbf{x_0}, t)\epsilon\mathbf{e_0}\| \approx \|\varepsilon\mathbf{e_0}\|e^{\lambda t}$$

for large t, where $\lambda = \lambda(\mathbf{x_0}, \varepsilon\mathbf{e_0})$. Thus, the Lyapunov exponent describes the exponential growth or decline rate of the perturbation.

The directional Lyapunov exponent $\lambda(\mathbf{x_0}, \varepsilon\mathbf{e_0})$ depends on the direction $\mathbf{e_0} \in \mathbb{R}^n$ of the initial perturbation. To characterize the most unstable behavior of the system, we define the maximal Lyapunov exponent as the supremum over all unit directions.

Definition 2.3.2 (Maximal Lyapunov Exponent)**.** *Let $\varphi(\mathbf{x_0}, t)$ be the flow map of a smooth dynamical system, and let $D\varphi(\mathbf{x_0}, t)$ be the Jacobian of the flow with respect to the initial condition $\mathbf{x_0}$. Then the **maximal Lyapunov exponent** at $\mathbf{x_0}$ is defined as*

$$\lambda_{\max}(\mathbf{x_0}) = \sup_{\|\mathbf{e_0}\|=1} \lambda(\mathbf{x_0}, \varepsilon\mathbf{e_0}),$$

where $\varepsilon\mathbf{e_0}$ is a small perturbation in the direction of the unit vector $\mathbf{e_0}$.

Remark 2.3.2. A positive maximal Lyapunov exponent, $\lambda_{\max}(\mathbf{x_0}) > 0$, indicates that there exists at least one direction in which nearby trajectories diverge exponentially. This is a signature of sensitive dependence on initial conditions (SDIC), and thus a strong indicator of chaotic behavior.

When the solution and thus the flow as well as the Jacobian of a system cannot be derived analytically, one can calculate the Finite-Time Lyapunov exponents as an approximation to Lyapunov exponents to check for sensitive dependence on initial conditions.

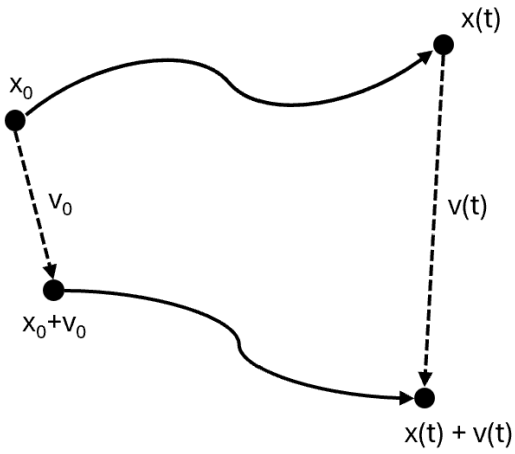

Figure 2.2.: Evolution of two initially nearby trajectories over time.

As before, for a perturbation vector $\mathbf{v_0} = \mathbf{v}(t_0)$ starting at $\mathbf{x_0}$, we know that it evolves like

$$\mathbf{v}(t) = D\varphi(\mathbf{x_0}, t)\mathbf{v_0}.$$

We are interested in the direction of the largest growth and write

$$\begin{aligned}\|\mathbf{v}(t)\| &= \sqrt{\langle D\varphi(\mathbf{x_0}, t)\mathbf{v}(t_0), D\varphi(\mathbf{x_0}, t)\mathbf{v}(t_0)\rangle} \\ &= \sqrt{\langle \mathbf{v_0}, D\varphi(\mathbf{x_0}, t)^T D\varphi(\mathbf{x_0}, t)\mathbf{v_0}\rangle} \\ &= \sqrt{\langle \mathbf{v_0}, C\mathbf{v_0}\rangle},\end{aligned}$$

where $C := D\varphi(\mathbf{x_0}, t)^T D\varphi(\mathbf{x_0}, t)$ is called the **Right Cauchy-Green Strain Tensor**. The direction of maximal stretching corresponds to the unit eigenvector $\mathbf{e_n}$ associated

with the largest eigenvalue λ_n of C. Then

$$\begin{aligned} C\mathbf{e_n} = \lambda_n \mathbf{e_n} \quad &\Leftrightarrow \quad \lambda_n = \langle \mathbf{e_n}, C\mathbf{e_n} \rangle \\ &\Rightarrow \quad \lambda_n = \frac{\|D\varphi(\mathbf{x_0}, t)\mathbf{e_n}\|^2}{\|\mathbf{e_n}\|^2}. \end{aligned}$$

Definition 2.3.3 (Finite-Time Lyapunov Exponent)**.** *[2] The term*

$$\max_{\mathbf{v_0}} \lambda_t(\mathbf{x_0}, \mathbf{v_0}) = \frac{1}{2t} \ln \lambda_n, \tag{2.1}$$

where

$$\lambda_t(\mathbf{x_0}, \mathbf{v_0}) = \frac{1}{t} \ln \left(\frac{\|D\varphi(\mathbf{x_0}, t)\mathbf{v_0}\|}{\|\mathbf{v_0}\|} \right),$$

is called the ***Finite-Time Lyapunov Exponent (FTLE)****.*

In practice, when one needs to rely on numerical computation of solutions, the matrix $D\varphi(\mathbf{x_0}, t)$ can be approximated by finite differences. Denote

$$\mathbf{x}(t) = \mathbf{x_0} + \int_0^t f(\mathbf{x}(\tau))d\tau =: \varphi_t(\mathbf{x_0}).$$

Then,

$$D\varphi_t(\mathbf{x_0}) = \begin{pmatrix} \frac{d\varphi_{t,1}}{dx_1} & \cdots & \frac{d\varphi_{t,1}}{dx_n} \\ \vdots & \ddots & \vdots \\ \frac{d\varphi_{t_n}}{dx_1} & \cdots & \frac{d\varphi_{t_n}}{dx_n} \end{pmatrix}$$

can be approximated by a central finite differencing scheme. For a small $\delta > 0$, denote $\delta_\mathbf{1} = (\delta, 0, \ldots, 0)$, $\delta_\mathbf{2} = (0, \delta, 0, \ldots, 0)$, and so on. Then the following matrix can be calculated numerically by using simulation data [15].

$$D\varphi_t(\mathbf{x_0}) \approx \begin{pmatrix} \frac{\varphi_{t,1}(\mathbf{x_0}+\delta_\mathbf{1})-\varphi_{t,1}(\mathbf{x_0}-\delta_\mathbf{1})}{|2\delta_\mathbf{1}|} & \cdots & \frac{\varphi_{t,1}(\mathbf{x_0}+\delta_\mathbf{n})-\varphi_{t,1}(\mathbf{x_0}-\delta_\mathbf{n})}{|2\delta_\mathbf{n}|} \\ \vdots & \ddots & \vdots \\ \frac{\varphi_{t,n}(\mathbf{x_0}+\delta_\mathbf{1})-\varphi_{t,n}(\mathbf{x_0}-\delta_\mathbf{1})}{|2\delta_\mathbf{1}|} & \cdots & \frac{\varphi_{t,n}(\mathbf{x_0}+\delta_\mathbf{n})-\varphi_{t,n}(\mathbf{x_0}-\delta_\mathbf{n})}{|2\delta_\mathbf{n}|} \end{pmatrix}$$

This matrix will be used to calculate the finite-difference approximation of the FTLE in equation (2.1).

Remark 2.3.3. Unlike classical Lyapunov exponents, which characterize the asymptotic behavior of dynamical systems, finite-time Lyapunov exponents are computed over a finite time interval and therefore depend explicitly on the chosen duration. This time

dependence introduces a challenge: Selecting an appropriate time horizon is not straightforward and often depends on the specific system and the dynamical features one aims to capture. For example, shorter durations may highlight transient structures, while longer durations may better reveal long-term behavior. As such, there is no universal rule for choosing an optimal time interval for FTLE computation, and the decision must be made with respect to the goals and constraints of the analysis [15].

2.4. Description of long-term dynamics

In nonlinear deterministic, finite-dimensional dynamical systems, all long-term attracting behavior typically falls into one of the following categories: fixed points, periodic orbits, quasiperiodic orbits and chaotic attractors [39]. These behaviors can be present in both discrete and continuous systems. Since we use Poincaré maps for analysing the behavior of our system, i.e. transform a continuous system into a discrete one, the definitions for these categories of behavior will be given for maps. In the following we will give a brief explanation for each of these behaviors.

2.4.1. Fixed points

Definition 2.4.1 (Fixed points)**.** *Consider a smooth map $F : \mathbb{R}^n \to \mathbb{R}^n$. We call* $\mathbf{x}$ *a* ***fixed point*** *of F if $F(\mathbf{x}) = \mathbf{x}$.*

Remark 2.4.1. In accordance to the definition of cyclic points in Definition 2.4.2, we also call a fixed point of a map **cyclic point of period 1**.

Remark 2.4.2. Note that by turning a continuous system into a discrete one (for example by constructing Poincaré maps), some behavior gets lost. In particular, if we have a fixed point of a map, this might on one hand correspond to a constant solution over time. On the other hand, a solution which is not constant over time, but returns to the same points exactly after one period of time (corresponding to one iteration of the map), will also show up as a fixed point of the map. However, for our applications, the seasonal variation in the systems equations prohibits constant solutions over time. So all points that appear as fixed points of the Poincaré map correspond to 1-year periodic solutions.

2.4.2. Periodic orbits

Definition 2.4.2 (Cyclic point)**.** *[3] Let $F : \mathbb{R}^n \to \mathbb{R}^n$ be a smooth map. We call* $\mathbf{x}$ *a* ***periodic*** *or* ***cyclic point of period*** $\mathbf{k}$ *if $F^k(\mathbf{x}) = \mathbf{x}$ and k is the smallest such integer.*

The orbit with initial point $\mathbf{x}$ *consists of* k *cyclic points and is called a* ***periodic orbit of period*** k*, or also* k***-cycle****.*

Orbits that converge to a periodic orbit after they lose all transience are called asymptotically periodic.

Definition 2.4.3 (Asymptotically periodic orbit)**.** *[3] Consider a smooth map* $F : \mathbb{R}^n \to \mathbb{R}^n$*. An orbit* $(\mathbf{x_1}, \mathbf{x_2}, \dots)$ *is called* ***asymptotically periodic*** *if there exists a periodic orbit of period* k*,* $(\mathbf{y_1}, \dots, \mathbf{y_k}, \mathbf{y_1}, \dots)$*, such that*

$$\lim_{n\to\infty} \|\mathbf{x_n} - \mathbf{y_n}\| = 0.$$

2.4.3. Quasiperiodic orbits

In contrast to periodic orbits of a certain period, trajectories belonging to quasiperiodic orbits do not return to the same spot after a certain time. The trajectories and the corresponding points in the Poincaré section form a closed curve or a dense set of points in our Poincaré section.

Definition 2.4.4 (Sensitive dependence on initial conditions)**.** *[2] A flow map* $\varphi : \mathbb{R}^n \to \mathbb{R}^n$ *has* ***sensitive dependence on initial conditions (SDIC)*** *if there exists a* $\delta > 0$ *such that for any initial condition* $\mathbf{x_0}$ *and any arbitrarily small neighborhood* $B_\varepsilon = \{\mathbf{y} | \, \|\mathbf{y} - \mathbf{x_0}\| < \varepsilon\}$ *with* $\varepsilon > 0$*, there exists a* $\mathbf{y_0} \in B_\varepsilon$ *and a time* τ *such that*

$$\|\varphi(\mathbf{x_0}, \tau) - \varphi(\mathbf{y_0}, \tau)\| > \delta.$$

Remark 2.4.3. In other words, SDIC means that the trajectories of two arbitrarily close points always end up at least δ apart for some time, no matter how close to each other they start.

Definition 2.4.5 (Quasiperiodic orbit)**.** *[3] A bounded orbit that is not asymptotically periodic and that does not exhibit sensitive dependence on initial conditions (SDIC) is called* ***quasiperiodic****.*

2.4.4. Chaos

Although there is no universally accepted definition of chaos, we give a definition that allows for a good working understanding.

Definition 2.4.6 (Chaos)**.** *[2, 3] In a deterministic system, a non-periodic orbit that exhibits sensitive dependence on initial conditions is called* ***chaotic orbit****.*

Remark 2.4.4. Recall Remark 2.3.1 for the Lyapunov exponent. If the Lyapunov exponent $\lambda > 0$ for a non-periodic point, we see that two initially nearby trajectories move apart from each other - which means that the system exhibits SDIC and thus the orbit is chaotic [40]. On the other hand, quasiperiodic orbits have Lyapunov exponents ≈ 0 and thus are neutral in some sense, i.e. they are neither attracting nor repelling [3].

Therefore, Lyapunov exponents (or FTLE) pose as a good indicator for SDIC [1].

3. Modeling

Seasonality plays a central role in shaping ecological dynamics in northern Fennoscandia, where long, snow-covered winters and short summers strongly influence food availability and species interactions [23]. In particular, small mammal predators such as mustelids adapt their foraging strategies to these seasonal changes, switching from generalist predation in summer to specializing on small rodents in winter [17]. To investigate how such seasonal shifts in predation behavior affect population dynamics, we aim to develop a minimal model that captures the interaction between predator and prey in a two-season environment.

Our approach builds on the framework introduced by Tyson and Lutscher [42], who used separate equations for summer and winter to reflect seasonal dynamics in a predator-prey system. While their model focused on owls and snowshoe hares, the underlying structure is well-suited to our system. Tyson and Lutscher proposed two modeling strategies: one involving discrete switching between the seasonal equations, and another using a time-averaged system where each equation is weighted by the fraction of the year it represents. While the latter offers a computationally simple approximation, it does not fully capture the temporal separation of seasonal behaviors.

In contrast, we introduce a continuous switching function - an approximation of a square wave - that smoothly transitions between summer and winter dynamics. This allows us to modulate the influence of each seasonal regime based on its relative duration while maintaining a continuous system. This continuity enables the use of bifurcation analysis and other mathematical tools [27]. To analyze the long-term, year-to-year dynamics, we introduce Poincaré sections, which provide a systematic way to represent the system's evolution on timescales exceeding the seasonal period.

3.1. Model description

3.1.1. Seasonal model equations

We introduce our model, which extends the seasonal framework proposed by Erbach et al. [11] and later developed by Tyson and Lutscher [42], using separate equations to describe predator-prey dynamics during summer and winter. The structure of our seasonal equations is identical to theirs, with the exception of adapted parameter values

and the inclusion of a winter reproduction term for the prey. The model we introduce in this section is also part of a manuscript currently in press [32].

Assume that summer occupies a fraction $0 \leq T_S \leq 1$ of the year. During this time, the prey population N grows logistically and reproduces independently of the predator P. We assume that resources are sufficient and that interspecific competition can be neglected. Deaths in the prey population are mainly caused by predation, so we include only this as a death term.

In summer, the predator population P is modeled as a generalist, following a Holling type III functional response [22]. It can grow independently of focal prey, assuming access to alternative resources, but its growth is enhanced when prey is abundant. Predator deaths are modeled as a linear term, independent of prey density.

The summer dynamics are given as

$$\frac{dN}{dt} = rN\left(1 - \frac{N}{K}\right) - \frac{aN^2P}{b^2 + N^2} \tag{3.1}$$

$$\frac{dP}{dt} = \gamma\frac{aN^2P}{b^2 + N^2} + \frac{sP}{1 + \nu P} - mP \tag{3.2}$$

In winter, that is, $T_W = 1 - T_S$, Tyson and Lutscher assume no reproduction of their focal prey (snowshoe hares). While most small rodent species breed primarily in summer, winter reproduction has been documented in several focal prey species, including lemmings and voles [6, 13, 38]. To account for this, we include a reproduction term for our focal prey N in winter that mirrors the summer reproduction, scaled by a factor c representing reduced reproductive activity.

As in summer, predation is the main source of mortality for the prey population. The predator P is assumed to specialize on the focal prey during winter, and its growth depends entirely on prey availability. We model this using a Holling type II functional response [11]. Predator deaths are again included as a linear term, independent of prey density.

The winter dynamics read as follows:

$$\frac{dN}{dt} = c\,rN\left(1 - \frac{N}{K}\right) - \frac{\alpha NP}{\beta N} \tag{3.3}$$

$$\frac{dP}{dt} = \gamma\frac{\alpha NP}{\beta N} - \mu P \tag{3.4}$$

For a more detailed description of the parameters as well as the values chosen for our rodent-mustelid system, see Table 3.1 in Chapter 3.2.

To simplify the analysis and identify the important parameter combinations, we introduce a nondimensionalization of the model like Tyson and Lutscher [42]. The prey

population is scaled by $\frac{1}{K}$ where K denotes its carrying capacity, while the predator population is normalized using the factor $\frac{rK}{a}$, which represents the ratio of the prey growth rate to the predator's maximum kill rate, leading to dimensionless prey and predator densities $n = \frac{N}{K}$ and $p = \frac{aP}{rK}$. Time is scaled by the intrinsic prey growth rate r, leading to a dimensionless time variable $\tau = tr$.

With these transformations, the seasonal model equations are expressed in terms of dimensionless population densities and time, allowing for a more general formulation of the seasonal dynamics. The exact nondimensionalization of the seasonal equations (3.1), (3.2), (3.3) and (3.4) is included in the Appendix A.

The nondimensional seasonal equations of our model then read as follows. First, the summer dynamics:

$$\frac{dn}{d\tau} = n(1-n) - \frac{n^2 p}{\tilde{b}^2 + n^2}, \tag{3.5}$$

$$\frac{dp}{d\tau} = \tilde{\gamma}\frac{n^2 p}{\tilde{b}^2 + n^2} + \tilde{s}\frac{p}{1+\tilde{\nu}p} - \tilde{m}p. \tag{3.6}$$

And the winter dynamics read as follows:

$$\frac{dn}{d\tau} = cn(1-n) - \tilde{\alpha}\frac{np}{\tilde{\beta}+n}, \tag{3.7}$$

$$\frac{dp}{d\tau} = \tilde{\gamma}\frac{\tilde{\alpha}np}{\tilde{\beta}+n} - \tilde{\mu}p. \tag{3.8}$$

3.1.2. Combining the seasonal equations to a single system

The next step is to transition from these piecewise seasonal model equations to a continuous formulation of the full dynamics. We introduce a smooth switching mechanism that connects summer and winter dynamics. By doing so, we preserve the distinct seasonal behaviors while ensuring a continuous right-hand side for the system, enabling us to apply a range of mathematical tools (and, in particular, bifurcation analysis).

We introduce the squdel function, which acts as a continuous approximation to a square-wave function. It is defined as follows [12].

$$sqd_s(t;\omega,\kappa) = \frac{\sin(\omega t)}{\sqrt{\sin^2(\omega t) + \kappa^2\cos^2(\omega t)}} \tag{3.9}$$

For $\kappa = 1$ the function is just the sine wave $\sin(\omega t)$ and if we let $\kappa \to 0$, we get a square function which alternates between -1 and 1 with period $1/\omega$. For this function to make sense in the context of seasons, we set $\omega = 2\pi/year$ (so that the period is exactly one full year).

In order to combine the squdel function with our seasonal nondimensional equations, we introduce the dimensionless quantity $\tilde{\omega} = \omega/r$, which in combination with $\tau = tr$ from before allows us to write the equation in a nondimensional way, so that the period still corresponds to $t = 1\,year$.

Furthermore, we want to rescale $sqd_s \in [-1, 1]$ to a squarewave function with values in $[0, 1]$, since this allows us to multiply the function with the seasonal dynamics in a suitable way to switch between summer and winter while still maintaining a continuous model. We introduce

$$f_s(\tau; \tilde{\omega}, \kappa) := \frac{1}{2}\left(1 + \frac{\sin(\tilde{\omega}\tau)}{\sqrt{\sin^2(\tilde{\omega}\tau) + \kappa^2 \cos^2(\tilde{\omega}\tau)}}\right) \tag{3.10}$$

and now use this switching function to combine the summer and winter dynamics into a single system. Since these seasonal dynamics are autonomous when considered separately, we can adjust their relative durations by scaling the corresponding vector fields. A longer summer, for example, can be modeled by speeding up the summer dynamics, which has the same effect as letting the system evolve for a longer time. Similarly, shortening winter corresponds to slowing down the winter dynamics. This speed rescaling is a standard technique in dynamical systems, often used to adjust the relative durations of different phases of an autonomous system [39].

For any summer length $T_S \in [0, 1]$, we combine the smooth seasonal switching function f_s and the rescaling factors for season length [1]

$$a_S = 2T_S \quad \text{and} \quad a_W = 2T_W = 2(1 - T_S) \tag{3.11}$$

with the nondimensional summer and winter models (Equations (3.5), (3.6), (3.7) and (3.8)). This gives us the full model for the predator-prey system of rodents and mustelids in northern Fennoscandia.

$$\begin{aligned}\frac{dn}{d\tau} =& a_S\, f_s(\tau; \tilde{\omega}, \kappa)\left[n(1-n) - \frac{n^2 p}{\tilde{b}^2 + n^2}\right] \\ &+ (2 - a_S)\,(1 - f_s(\tau; \tilde{\omega}, \kappa))\left[cn(1-n) - \tilde{\alpha}\frac{np}{\tilde{\beta} + n}\right]\end{aligned} \tag{3.12}$$

$$\begin{aligned}\frac{dp}{d\tau} =& a_S\, f_s(\tau; \tilde{\omega}, \kappa)\left[\tilde{\gamma}\frac{n^2 p}{\tilde{b}^2 + n^2} + \tilde{s}\frac{p}{1 + \tilde{\nu}p} - \tilde{m}p\right] \\ &+ (2 - a_S)\,(1 - f_s(\tau; \tilde{\omega}, \kappa))\left[\tilde{\gamma}\frac{\tilde{\alpha}np}{\tilde{\beta} + n} - \tilde{\mu}p\right]\end{aligned} \tag{3.13}$$

[1] See Appendix A for details.

3.1.3. Embedding the system in a higher-dimensional setting

In order to analyze the year-to-year dynamics of our system, we want to implement a Poincaré section, for which we need to have an autonomous system of differential equations. So far, the right-hand side of our system (3.12) and (3.13) is explicitly dependent on τ and is therefore non-autonomous. However, we can solve this problem quite easily (see Proposition 2.1.1): we embed the system in the three-dimensional phase space prey-predator-time. So far, our system has been of the form

$$\dot{x}(t) = \begin{pmatrix} \dot{n}(\tau) \\ \dot{p}(\tau) \end{pmatrix} = \frac{d}{d\tau} x(\tau) = f(\tau, x(\tau)), \quad x(0) = x_0,$$

where

$$x(\tau) = \begin{pmatrix} n(\tau) \\ p(\tau) \end{pmatrix}.$$

This is equivalent to

$$\begin{pmatrix} \dot{n} \\ \dot{p} \\ \dot{\tau} \end{pmatrix} = \begin{pmatrix} f\left(\tau, (n,p)^T\right) \\ 1 \end{pmatrix}, \quad \begin{pmatrix} n \\ p \\ \tau \end{pmatrix}(0) = \begin{pmatrix} n_0 \\ p_0 \\ 0 \end{pmatrix},$$

thus, we can rewrite our system of equations as an autonomous system in the extended prey-predator-time phase space.

$$\begin{pmatrix} \dot{n} \\ \dot{p} \\ \dot{\tau} \end{pmatrix} = \begin{pmatrix} a_S\, f_s(\tau;\tilde{\omega},\kappa)\left[n(1-n) - \frac{n^2 p}{\tilde{b}^2+n^2}\right] + (2-a_S)\,(1-f_s(\tau;\tilde{\omega},\kappa))\left[cn(1-n) - \tilde{\alpha}\frac{np}{\tilde{\beta}+n}\right] \\ a_S\, f_s(\tau;\tilde{\omega},\kappa)\left[\tilde{\gamma}\frac{n^2 p}{\tilde{b}^2+n^2} + \tilde{s}\frac{p}{1+\tilde{\nu}p} - \tilde{m}p\right] + (2-a_S)\,(1-f_s(\tau;\tilde{\omega},\kappa))\left[\tilde{\gamma}\frac{\tilde{\alpha}np}{\tilde{\beta}+n} - \tilde{\mu}p\right] \\ 1 \end{pmatrix}, \tag{3.14}$$

3.2. Parameter choices

3.2.1. Model parameters

As our seasonal model equations closely follow the structure introduced by Tyson and Lutscher [42], we adopt a similar set of parameters in terms of their functional roles and interpretations. However, since our study focuses on a different predator-prey system - namely, small rodents (Norwegian lemming *Lemmus lemmus*, grey-sided vole *Myodes rufocanus*, field vole *Microtus agrestis*, and tundra vole *Alexandromys oeconomus*) as prey, and mustelids (least weasel *Mustela nivalis nivalis* and stoat *Mustela erminea*) as predators [21] - the numerical values of these parameters have been adjusted accordingly.

Param.	Description	Unit	Range	Ref.	Value used
r	Prey summer growth rate	Per year	4-7	[17, 41]	5.4
K	Prey summer carrying capacity	Voles/ha	100-200	[17, 41]	100
α	Specialist saturation killing rate	Voles/year/weasel	500-700	[17, 41]	600
β	Specialist half-saturation	Voles/ha	1-14.5	[25, 41]	13
γ	Predator-prey ratio constant	Weasel/voles	0.017-0.05	[25, 41]	0.017
s	Predator max growth rate	Per year	1-1.6	[17, 41]	1.6
m	Generalist death rate	Per year	0.82-0.66	[25, 29]	1.0
μ	Specialist mortality	Per year	0.9-1	[25]	3.4
a	Generalist saturation killing rate	Voles/ha/year	70-200	[41]	70
b	Generalist half-saturation	Voles/ha	13.8	[41]	13
c	Winter prey reproduction factor	Per year	0-78%	[6, 35]	0.4
ν	Generalist predator density dependence	Per weasel	unknown		

Table 3.1.: Parameter value ranges for the rodent-mustelid model in dimensional form [32]. In this table, 'vole' denotes all prey species and 'weasel' denotes all predator species as described in the text. Area measurements are given in hectares (ha).

The parameters used in our model, along with their biological interpretations and units, are summarized in Table 3.1.

For a detailed description and discussion of parameter choices, we refer to [32].

The generalist predator density dependence ν is a parameter that was introduced by Tyson and Lutscher for the dynamics of the great horned owl and the snowshoe hare [42]. Estimating this parameter is a very challenging task in general and has not yet been done for the rodent-mustelid system. Therefore, we aim to include ν as a second bifurcation parameter (in addition to the summer length, or more precisely, $a_S = 2T_S$) and investigate its impact on the long-term dynamics of our system.

3.2.2. Parameters for the switching function

In reality, seasonal transitions are never perfectly discrete - there is no sudden, instantaneous switch between summer and winter. However, in northern Fennoscandia, these transitions tend to occur relatively quickly due to the sharply defined seasonal climate of the region [24]. In our simulations, we chose a value of $\kappa = 0.001$ for the switching function f_s (see Equation (3.10)), which produces a very steep, nearly squarewave-like transition between seasons. While this may slightly overestimate the speed of seasonal change in nature, it allows us to clearly separate summer and winter dynamics within the model, which is useful for both interpretation and analysis.

3.2.3. Parameters for the Poincaré section

Because our switching function f_s has period r (as $\tau = tr$ for period $t = 1$), we need to introduce r-periodic Poincaré sections in order to capture one data point at the same time each year. Furthermore, since summer lasts from $\tau = 0$ to $\tau = 0.5r \pmod{k}$, and our switching function is not a perfect square wave, but has a rather steep slope at τ close to 0 and $0.5r$, we decide to keep the Poincaré section away from the slopes and set it in the middle of summer, that is, at $\tau_{poinc} = 0.25r$.

4. Classifying long-term dynamics

The first major objective is to classify all attracting long-term behavior that is present for a certain combination of parameters. We want to determine whether there exist multiple attractors and define their types (periodic, quasiperiodic or chaotic).

Getting an exact analytical solution of our system for a general initial condition is not feasible due to the complicated structure. Therefore, we need to compute the solution trajectories for each initial condition numerically in simulations. So, in order to capture all the (potentially coexisting) long-term attractors of a system, we proceed as follows. We create a grid of initial conditions spread across the whole predator-prey space and compute the solution trajectories for all of them. If the simulation runs for a long time, the transience gets lost and all trajectories will converge to attracting orbits.

If we choose the initial grid fine enough, and assuming that the basins of attraction are not too small or fragmented, we can reasonably expect to capture all long-term attractors present in the system. This is because the system of ODEs is continuous, so nearby initial conditions lead to similar trajectories. While this approach cannot ensure that every attractor is detected - especially in systems with complex dynamics - it remains a widely used and practical method for exploring the long-term behavior of such models.

In this thesis, we will always use a 10×10 grid of initial conditions, leading to 100 trajectories, which allows us to capture the dominant attractors while maintaining a balance with computational resources.

What remains is to classify all the attracting orbits - i.e. determine their type. For this, we come up with a novel classification algorithm that takes a (potentially large) number of simulation trajectories and not only classifies the types of all the attracting structures, but also the periods of the periodic orbits (if there exist any) and the exact locations of all attractors. The following section is also included in a manuscript, currently in press [32].

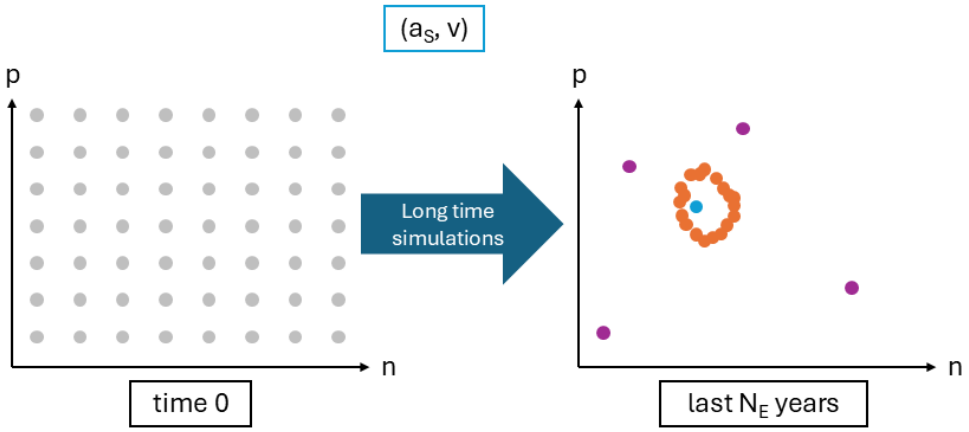

Figure 4.1.: Attracting structures in a long-time simulation for a grid of initial conditions.

4.1. The classification algorithm

The classification algorithm consists of three distinct steps.

First, all 100 trajectories are grouped into clusters. Each cluster consists of those trajectories that share the most similarities. In order to do this, we use the clustering algorithm described in [14] which works as follows.

We construct a similarity matrix of a weighted graph (with our trajectories as nodes and similarities as edges[1]). The similarity between two trajectories is inversely proportional to the sum of the Euclidean distances between those two trajectories for each timestep in the last N years. This means that two trajectories whose euclidean distances are small share a high similarity.

This similarity matrix is then used to solve a generalized eigenvalue problem. The location of the largest gap between two subsequent eigenvalues (which are ordered by size) indicates the optimal number of clusters. The idea behind this approach comes from graph theory, where in a perfect graph, the number of connected components corresponds to the number of zero-eigenvalues in the similarity matrix [34]. The connected components can be viewed as groups of trajectories that are very similar to each other, and thus the number of connected components is also the optimal number of clusters.

The clusters themselves are then calculated using the k-means clustering algorithm, which iteratively allocates the trajectories to the clusters with respect to their similarities. This gives a list of length 100 that indicates the cluster to which each trajectory belongs - so the one where it has the most similarity to the other members in the group.

[1] Here we restrict ourselves to taking the last $N = 50$ years in the Poincaré section for every trajectory, as we are just interested in the attracting long-term behavior rather than the initial transient phase.

In the presence of chaos, one can expect many different clusters, as the trajectories do not stay close to each other.

In the second step, we categorize each cluster's behavior. We select only one representative trajectory for each of the k clusters, as all the trajectories within the same cluster are very similar to it. Then, we check the representatives for periodicity - if a trajectory returns to the same point after a finite number m of years, we classify the corresponding cluster as periodic with period m.

If the clustering algorithm classified two clusters as distinct, yet their representative trajectories intersect at the same cyclic points, we group those two clusters together. For example, if our predator-prey system has a 4-cycle at locations A-D, the initial clustering algorithm will distinguish between trajectories starting at $(A, B, C, D, A, \dots)$ and $(B, C, D, A, B, \dots)$. Those two clusters clearly belong to the same periodic orbit (as they visit the same locations in the same ordering) and thus get grouped together into a new common cluster.

All non-periodic representatives of clusters belong to either a quasiperiodic orbit or chaotic behavior. Determining which of these two behaviors the trajectory (and therefore its cluster) belongs to, will be the third step in our algorithm.

The third step is to distinguish between quasiperiodic orbits and chaos. As described in Remark 2.4.4, a positive largest Lyapunov exponent indicates sensitive dependence on initial conditions (SDIC), and therefore chaos. Due to the structure of our system of ODEs, we used a finite-difference approximation to compute the Jacobian. As described in [15] and Chapter 2.3, this approximation can also be used when calculating the Finite-Time Lyapunov Exponents (FTLE). A positive FTLE value indicates SDIC, thus serving as an indicator for chaos.

Quasiperiodic orbits are characterized by trajectories that neither exponentially converge nor diverge, resulting in Lyapunov exponents close to zero (see Remark 2.4.4). However, due to numerical errors, FTLE values will never be exactly zero in simulations. To distinguish between chaotic and quasiperiodic behavior, we introduce a threshold.[2]

Additionally, since FTLE values explicitly depend on the time interval over which they are computed, we calculate them over a range of durations (from 50 to 59 years[3]) and take the median of these values. This helps to smooth out fluctuations and provides a more robust estimate of the system's sensitivity to initial conditions.

[2] Preliminary simulations across various parameter combinations suggested that a threshold of 0.01 provides a reliable distinction between chaos and quasiperiodicity.

[3] By choosing to compute the FTLE for these durations, we limit the impact of initial fluctuations, while also ensuring that the FTLE values are still large enough to allow for a meaningful distinction for SDIC. In practice, however, choosing the optimal time for which FTLE are computed depends on the application and the system; see Remark 2.3.3.

Using this approach, we select a random point from the trajectory under consideration[4], compute the FTLE values across the chosen time intervals, take the median, and compare it to the threshold. If the median lies below the threshold, we classify the trajectory as quasiperiodic; otherwise, if the median FTLE is significantly positive, we classify it as chaotic.

As we rely on thresholds in both the second and third steps of our classification algorithm, minor noise can occur due to numerical errors. These cases were double-checked and manually corrected if necessary.

This algorithm allows us to classify different long-term behaviors from the trajectories produced in our simulations, even when multiple qualitatively different behaviors coexist.[5] Figure 4.2 shows the final result for an example scenario.

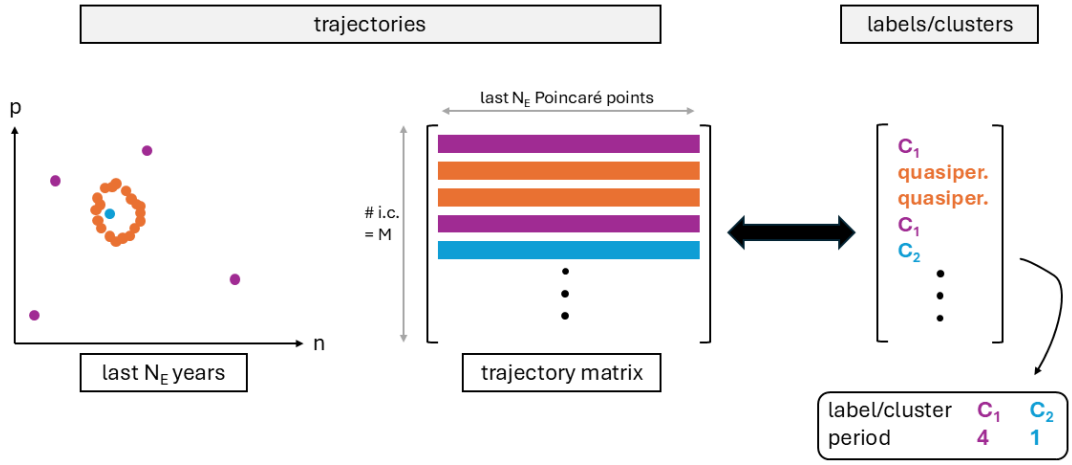

Figure 4.2.: Result of the classification algorithm for an example scenario.

[4] When the randomly selected trajectory point lies very close to the coordinate axes (i.e., with very low predator or prey densities), the finite-difference step size used for the Jacobian approximation must be very small. This can reduce the robustness of the FTLE calculation and amplify numerical errors. While this does not qualitatively affect our classification, it can occasionally produce spurious values and should be kept in mind when interpreting results.

[5] Note that we did not allow for coexisting chaotic and quasiperiodic behavior in the classification algorithm. While such coexistence is theoretically possible in nonlinear dynamical systems (see, e.g., [7]), we did not observe clear evidence of it in our simulations. This simplification was made to ensure robustness and interpretability of the classification algorithm.

4.2. Example results

The classification algorithm can now be applied to simulations of our system (3.14). In Figure 4.3, some examples for different attracting behavior are given. The simulations were performed for 5000 years each and only the last 50 points in the Poincaré map for each trajectory were plotted. This choice ensures that all transient behavior is lost and only the long-term attractors are left.[6]

We see that for different combinations of summer length (or more precise, a_S) and generalist density dependence ν, we get qualitatively very distinct behaviors, allowing for multiple of the above mentioned behaviors (chaos, quasiperiodic orbits, cyclic points) to be present at the same time. If two (or more) different attractors are present simultaneously, this means that some of the initial conditions lead to convergence to the first attractor and the others to the other attractor.

Additional simulations were also conducted for the limiting cases $a_S = 0$ and $a_S = 2$, where only the winter or summer equation is active, respectively. These results are discussed in Appendix B and provide further insight into the role of single-season dynamics in shaping the full combined dynamics of the system.

With these results, it is natural to ask for a better overview of long-term behaviors - in which areas of values of a_S and ν does which type of behavior occur? This question leads to the creation of a two-dimensional bifurcation diagram with bifurcation parameters a_S and ν in the next chapter.

[6] In some cases, a shorter simulation time would also be sufficient to lose all transient behavior, but to keep the simulations consistent for each parameter combination, this choice of 5000 years was made.

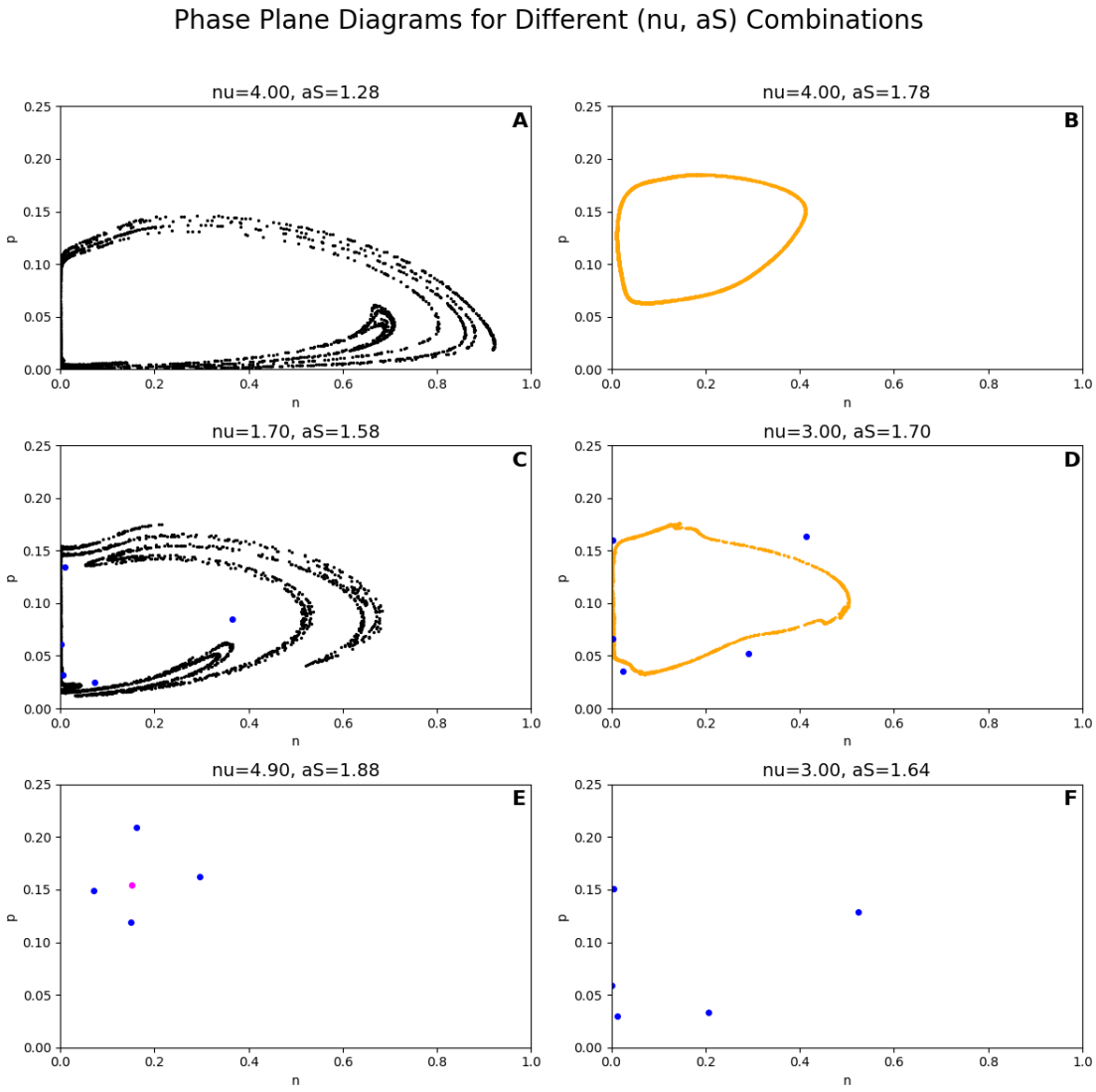

Figure 4.3.: Examples for different long-term attracting structures in the Poincaré section depending on the choice of parameters a_S and ν. A: chaotic orbit, B: quasiperiodic orbit, C: coexisting chaotic orbit and 5-cycle, D: coexisting quasiperiodic orbit and 5-cycle, E: coexisting 4- and 1-cycle, F: 5-cycle.

5. Bifurcations and 2D bifurcation diagram

5.1. Bifurcation diagrams

In dynamical systems, bifurcation diagrams are a widely used graphical representation to illustrate how the behavior of a system changes when a parameter is varied. A sudden change in behavior when a parameter is smoothly varied is called **bifurcation** and the parameter is called **bifurcation parameter** [3]. Typically, in such a one-dimensional bifurcation diagram the horizontal axis represents a bifurcation parameter, while the vertical axis describes the sytem's long-term dynamics (such as fixed points, cycles or chaos).

When not only the changes in one parameter are relevant, one can also describe the qualitative changes in long-term behavior in higher-dimensional bifurcation diagrams (we will limit ourselves to the two-dimensional case) [27]. Proceeding like in [37], the bifurcation diagram partitions the parameter plane (with one bifurcation parameter on the horizontal axis and one on the vertical axis) into regions, where the system exhibits different qualitative behavior. The borders between two such areas correspond to bifurcations, where the type of bifurcation remains the same for every point along the curve.

To investigate both the impact of seasonal forcing and the strength of generalist density dependence (ν), we want to come up with a two-dimensional bifurcation diagram. However, since we are numerically simulating the dynamics, exact analytical 2D bifurcation diagrams cannot be constructed. We aim to approximate this numerically by creating a grid in the 2D a_S-ν space, simulating and classifying the long-term behavior for each parameter combination, and visualize areas of distinct qualitative behavior using different colors.

In order to capture all (relevant) behavior, it is important to choose the grid fine enough. However, as it lies in the nature of bifurcations, they appear suddenly and therefore we cannot guarantee that we find all distinct areas of qualitative behaviors in our numerical bifurcation diagram. Still, the bifurcation diagram captures the major areas of qualitatively different behavior and thus gives a good overview for our purposes.[1]

[1] Putting it in an ecological context, very small areas of qualitatively different behavior are very unlikely to appear in real-life scenarios, as there will always be small fluctuations in parameter values which makes it unfeasible that the system stays at this region of parameters for a long time.

5.2. The numerical 2D bifurcation diagram

The following description of the parameter ranges and simulation approach builds on our previous work [32]. As described in section 5.1, we construct a numerical two-dimensional bifurcation diagram for a grid of a_S and ν values. We use steps of size 0.02 in a_S (which corresponds to 3.65 days) and steps of size 0.1 in ν. Initial simulations suggested that the interesting behavior is contained in the right a_S half-plane. Therefore, we choose $a_S \in [1.0, 2.0]$. Generalist density dependence ν cannot be negative and thus we set the range $\nu \in [0.1, 6.0]$, as this allows us to capture the most interesting behaviors.

For each combination of a_S and ν, we create a 10×10 grid of initial conditions spread equally across the (n, p) phase plane.[2] We obtain the numerical solution for all these initial conditions and use the last 50 entries of the Poincaré sections (out of 5000 years simulation data) of each of those trajectories in the (n, p) phase plane. Then the classification algorithm described in Chapter 4.1 is applied, classifying all the present long term behavior for all the combinations of a_S and ν in the grid for our numerical bifurcation diagram.

Using those results, we visualize the areas of different qualitative behavior as different categories with certain colors. Each border between two distinct regions corresponds to a bifurcation.

The bifurcation diagram is given in Figure 5.1. We see that a large part on the left (i.e. for relatively low values of a_S) consists of chaos only or chaos coexisting with some cyclic points. Examples for these chaotic folds can be seen in Figure 4.3 A (where we have chaotic folds only) and in Figure 4.3 C (where we have a 5-cycle present in addition to chaotic folds). For larger values of a_S, we have multi-year cycles (in orange), quasiperiodic orbits (in turquoise, or light green when coexisting with cyclic points) and single-year cycles (in red). The different regions will be discussed in detail below.

A closer investigation of the types of bifurcations in the diagram helps to clarify the mechanisms driving the transitions between different dynamical behaviors. Understanding these bifurcation types provides a foundation for interpreting the broader structure of the diagram and for later analysis of transition speeds and tipping points (see Chapter 7).

For high values of a_S, we see a large red area where we have one-year periodic solutions (1-cycles) only. By decreasing a_S, quasiperiodic orbits emerge from these 1-cycles (see Figure 5.2). This is indicative of a **Neimark-Sacker bifurcation**:

[2] We spread them across $[0.01, 1.0] \times [0.01, 0.2]$ as this seems to be the relevant initial parameter space to capture all the dynamics. Higher p values for the initial grid lead to the same long-term attractors and therefore do not need to be included.

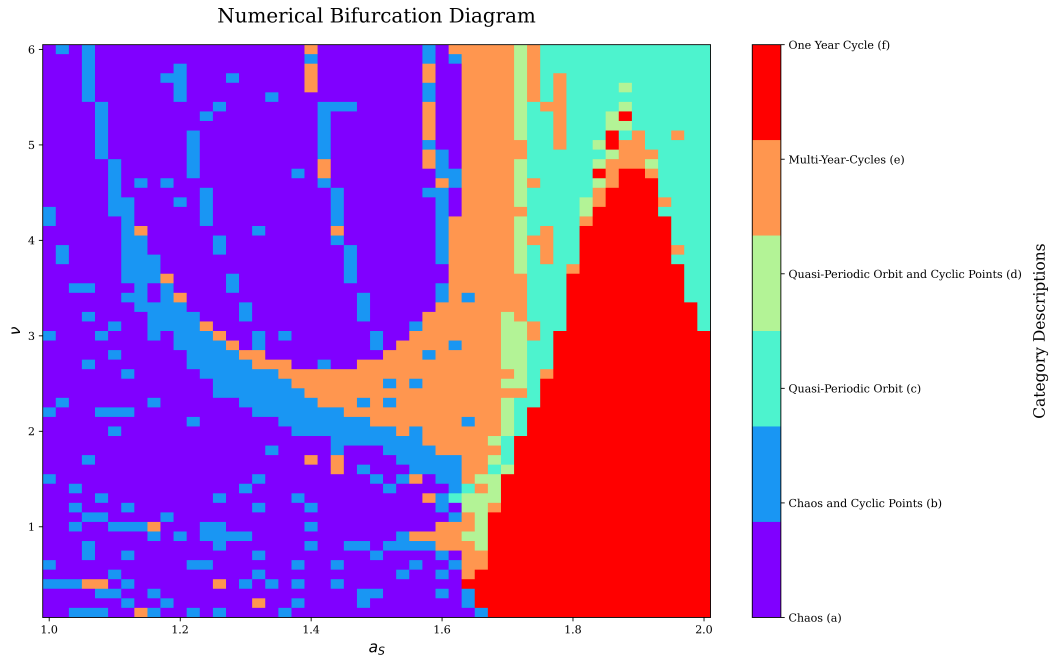

Figure 5.1.: Numerical 2D Bifurcation diagram for our system [32]. The colors describe the different regions of distinct qualitative behavior. a: chaos, b: coexisting chaos and periodic orbits, c: quasiperiodic orbit, d: coexisting quasiperiodic orbit and (at least one) cycle, e: (at least one) cycle of period more than one year, f: a single one year cycle.

Definition 5.2.1 (Neimark-Sacker bifurcation)**.** *[40] A* ***Neimark-Sacker bifurcation*** *occurs in discrete-time dynamical systems (i.e. maps) when a fixed point loses stability as a pair of complex conjugate eigenvalues of the Jacobian cross the unit circle in the complex plane. This bifurcation leads to the emergence of a closed invariant curve (a torus in the Poincaré map), resulting in quasiperiodic motion on that curve.*

Remark 5.2.1. The Neimark-Sacker bifurcation is the discrete-time equivalent to a Hopf bifurcation. Therefore it is also called secondary Hopf bifurcation [40].

Indeed, numerical simulations support this claim. When choosing a fixed ν, starting far in the red area where we have 1-cycles and while decreasing a_S calculating the stability of the 1-cyclic point for each of the a_S, we see that the modulus of the eigenvalues approaches 1. The pair of eigenvalues of the Jacobian crosses the unit circle right at the point where the cyclic point disappears and the quasiperiodic orbit appears.

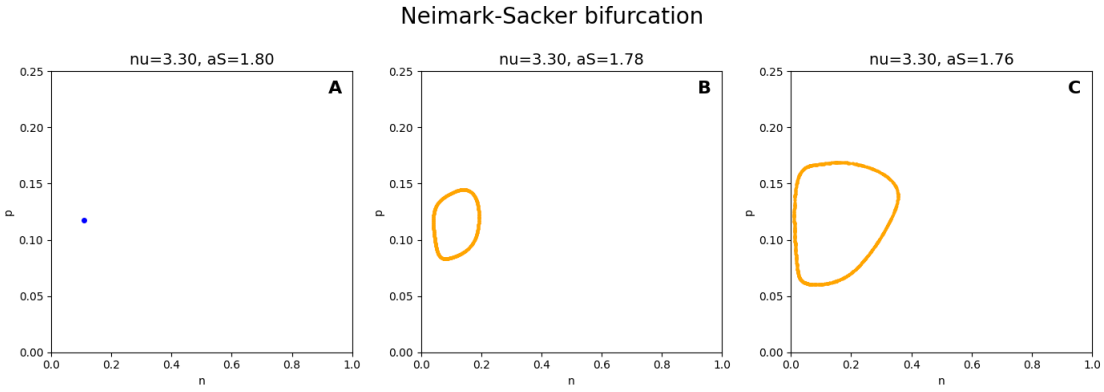

Figure 5.2.: Neimark-Sacker bifurcation. The fixed point of the Poincaré map (1-year cycle) loses its stability and a quasiperiodic orbit emerges (from A to C).

Remark 5.2.2. Note that the definition for a Neimark-Sacker bifurcation also holds for k-periodic orbits, not only for a 1-cycle. In that case, k tori appear in the Poincaré section where the k cyclic points used to be before stability was lost.

Areas where only cyclic points (of period greater than 1 year) are present are denoted in orange. In our system, we mostly have 5- and 6-year periodic cycles as well as period-doubled cycles of those. Looking at the wide orange band for $a_S \in [1.64, 1.7]$ and starting on the right, we have only 5-year cyclic points present. Decreasing a_S leads to a period doubling, thus splitting those 5 points into 10. Continuing to decrease a_S, the periods double again and once we transition to the purple area (i.e. only chaos), we first end up with five stretches of chaotic behavior. We call this **small band chaos**. Decreasing a_S further, those chaotic stretches turn into a chaotic fold behavior, which fills a large part of the phase space. This whole transition from 5-cycles to chaos can be described as **period doubling to chaos** and can be seen in Figure 5.3.

Definition 5.2.2 (Period-doubling bifurcation)**.** *[3] A* ***period-doubling bifurcation*** *occurs when a periodic orbit of period k becomes unstable and gives rise to a new stable orbit of period $2k$. This process can repeat recursively, leading to a cascade of bifurcations, with each new orbit having twice the period of the previous one. As the bifurcation parameter approaches a critical value, the periods of the orbits become infinitely long, and the system transitions to chaotic behavior.*

Remark 5.2.3. The period-doubling route to chaos is one of the most common and well-studied mechanisms by which deterministic systems exhibit chaos [3]. Within the period-doubling cascade, regions of chaotic behavior can also be interrupted by ranges of cyclic behavior [40].

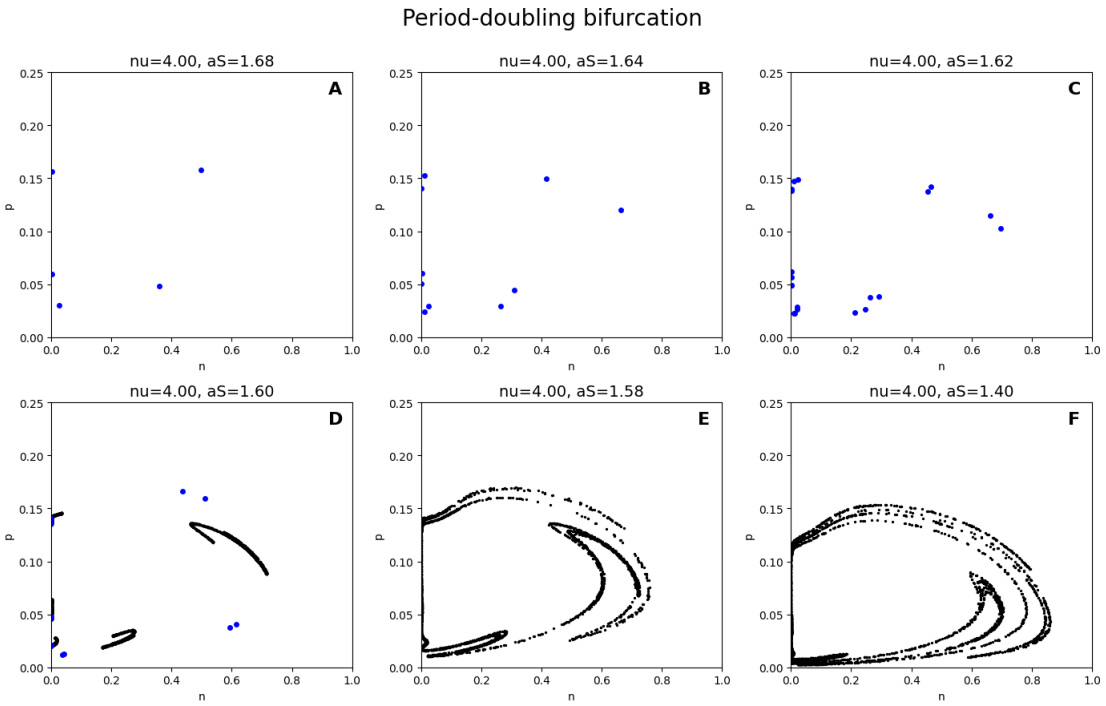

Figure 5.3.: Period-doubling bifurcation. The 5-cycle (A) splits into a 10-cycle (B), then into a 20-cycle (C) before turning into small-band chaos (D). Subsequently, this behavior turns into 'full' chaotic folds (E and F). Note, that the additional 12-cycle in D is part of a base-6 period-doubling and emerges on totally different areas than the 5-cycle or its period-doubled attractors.

The other big orange area of cyclic points with a period greater than 1 year - around $\nu \in [2, 3]$ and for intermediate $a_S \in [1.3, 1.62]$ - also consists of 5-cyclic points and their subsequent period-doubled cycles (again, the period doubling occurs moving from high a_S to low a_S). The intermediate points of chaos are mostly just small band chaos, but also stretches where we get additional noise from a 6-year cyclic period doubling cascade. This 6-year period doubling happens at multiple small bands (visible as small blue- and orange flares in the purple sea of chaos) and as mentioned can also be present additionally to the 5-year cyclic points or their period doubled cycles.

Next, we look at the transitions from turquoise (quasiperiodic orbit only) via light green (quasiperiodic orbit and cyclic points) to orange (cyclic points only). Focusing on $\nu > 2$, so where we have more or less vertical separation of the areas, we start at the turquoise area (for large a_S). Decreasing a_S and keeping ν constant, the quasiperiodic orbit expands and at some point, outside of the quasiperiodic orbit, a 5-year cycle appears (that is, five cyclic points). Increasing a_S further, the quasiperiodic orbit and those five cyclic points move closer to each other and, at some point, those two limiting structures collide, leaving only the 5-cycle as attracting long-time behavior.

There are two types of bifurcation within this transition: the emergence of additional 5-cyclic points to a quasiperiodic orbit (from turquoise to light green) is a **saddle-node bifurcation** for a 5-cycle (see Figure 5.4), and moving from light green to orange, we have **collision** of attractors (see Figure 5.5).

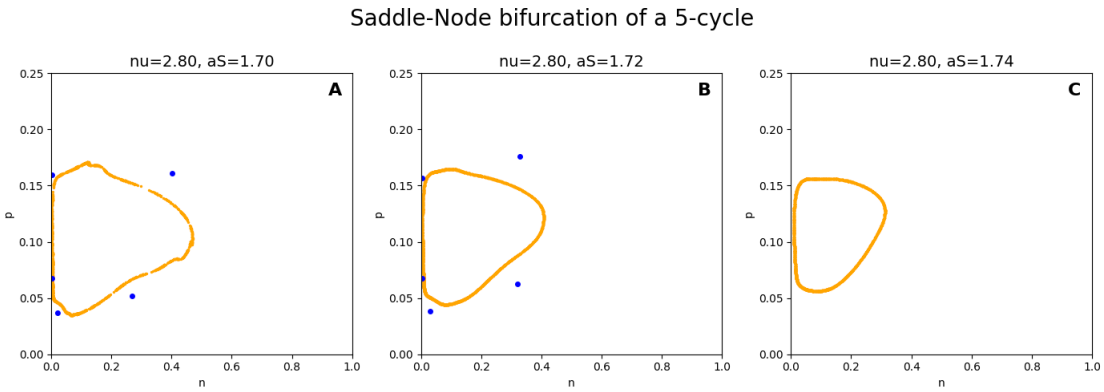

Figure 5.4.: Saddle-node bifurcation. The stable 5-cycle loses its stability due to collision with an unstable 5-cycle and leaves a quasiperiodic orbit as the sole attractor (A to C).

Definition 5.2.3 (Saddle-node bifurcation for k-cycles)**.** *[3] A **saddle-node bifurcation for k-cycles** occurs when a pair of periodic orbits of period k - one stable and one unstable - collide and annihilate each other as the bifurcation parameter is varied.*

Remark 5.2.4. This is a generalization of the saddle-node bifurcation for fixed points to periodic orbits. In the bifurcation diagram, this typically occurs as the sudden appearance or disappearance of a k-periodic orbit, as the unstable k-periodic orbit is not visible in long-term forward-in-time simulations.

In our case, starting in the light-green area of coexisting quasiperiodic behavior and a 5-cycle and increasing the bifurcation parameter, the stable k-cycle loses its stability (as it collides with the - forward-in-time hidden - unstable k-cycle) and disappears as they annihilate each other. Numerical stability analysis along this 5-cycle supports our claim.

Definition 5.2.4 (Collision of attractors)**.** *When two invariant sets, such as a quasiperiodic orbit and a periodic orbit, approach each other in phase space and eventually collide, leading to a qualitative change in the system's dynamics, we call this **collision bifurcation**. After the collision, one of the structures (often the quasiperiodic orbit) disappears, and the other (e.g., a periodic orbit) becomes the dominant attractor.*

Remark 5.2.5. Although often mentioned in literature on bifurcation theory, for example

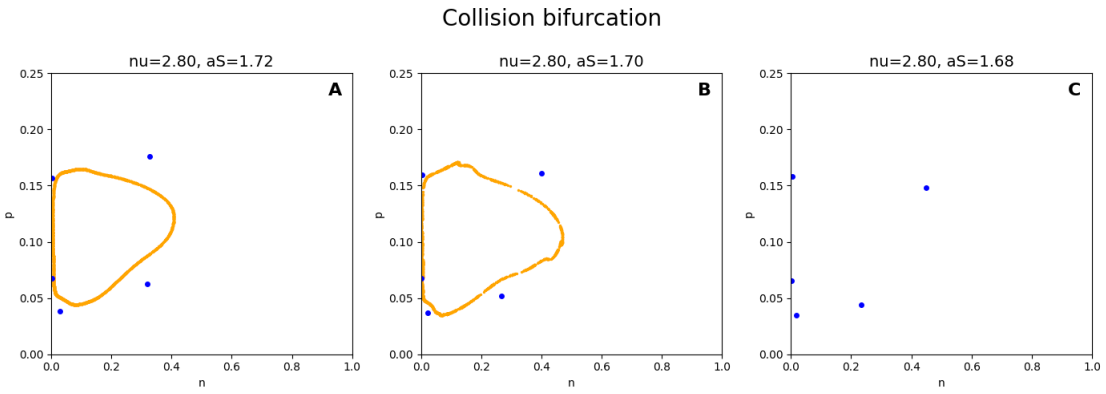

Figure 5.5.: Collision bifurcation. The five-cycle and the quasiperiodic orbit move closer to each other and collide, leaving only the 5-cycle as an attracting structure (A to C).

in [3], there is no consistent name for this behavior. We chose to call it **collision bifurcation** as this gives a very good intuition of what this bifurcation type is about.

Now focus at the area of low ν values and $a_S \in [1.6, 1.68]$. For low values of a_S, so starting in the purple area, we have a chaotic attractor only. Then, by increasing a_S, suddenly a stable 1-year cyclic point appears inside of these chaotic folds and they coexist. As we increase a_S even further, the basin of attraction of this fixed point expands to the point that it collides with the chaotic attractor [3] and therefore the chaotic attractor suddenly disappears. This collision of the basin of attraction and the disappearance of the chaotic attractor (see Figure 5.6) is due to a **boundary crisis bifurcation**.

Definition 5.2.5 (boundary crisis bifurcation)**.** *[3] A* ***boundary crisis bifurcation*** *occurs when a chaotic attractor collides with the edge of its basin of attraction. This collision typically leads to the abrupt disappearance of the attractor.*

Similarly, the transition from 5-cyclic points to the additional emergence of chaotic folds, to the disappearance of the 5-cyclic points and only the chaotic folds being present (orange to blue to purple for $\nu \in [1.5, 2]$ and $a_S \in [1.52, 1.64]$) can be described by a boundary crisis bifurcation as well. The only difference is that we have a 5-cycle instead of a yearly cycle. The stability analysis of the 5-cyclic points and the FTLE values of points on the chaotic folds support our claim.

One of the two remaining regions of interest is the area that looks like the tip of the

[3] Or in other words: the basin of attraction of this chaotic attractor (which borders the basin of attraction of the cyclic point) gets pushed out to the point that it collides with the chaotic attractor itself.

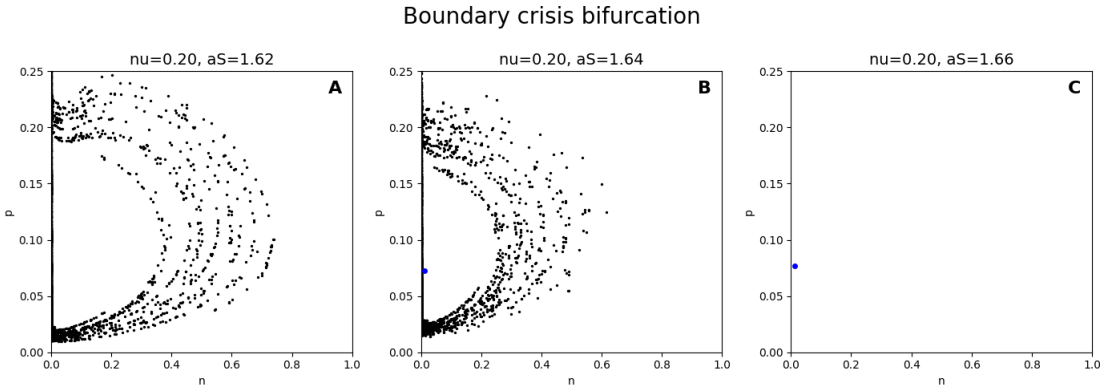

Figure 5.6.: Boundary crisis bifurcation. A fixed point in the Poincaré map emerges within chaotic folds, as it gains stability. Its basin of attraction then spreads so far, that the chaotic folds collide with their basin of attraction, leaving the 1-cycle as the only stable attractor in the system (A to C).

red mountain of 1-cycles - that is, $\nu \in [4, 5.5]$ and $a_S \in [1.82, 1.96]$. This area is very fascinating because we have numerous different combinations of the below (see Figure C.2 in the Appendix for some examples). The appearance of the 4-cyclic points can be explained with the saddle-node bifurcation of cycles (since they gain stability there). The transition from 4-cyclic points to 4 quasiperiodic orbits emerging from those 4 cyclic points is mathematically the same as the classical Neimark-Sacker bifurcation, but just with 4 instead of 1 points/orbits now.

All this behavior can therefore be explained as combinations of a saddle-node bifurcation of a 4-cycle, Neimark-Sacker bifurcations of a 1-year and of a 4-year cycle and collisions of orbits.

The last region we want to highlight is the area around $\nu \in [0.5, 2]$ and $a_S \in [1.6, 1.7]$. There we have the most manifold combination of long-term behavior. It is difficult to keep an overview; all the different behaviors connect in this area. However, essentially it can all be explained as various combinations of all the bifurcation archetypes that we defined, namely the following: Appearance of 1-, 5-, and 6-cyclic points due to gaining stability (saddle-node bifurcation), Neimark-Sacker bifurcation on 1-, 5- and 6-cyclic points, collision of orbits, period doubling and crisis bifurcation.

Examples of combinations of behaviors within this maze of bifurcations can be seen in Figure C.1 in the Appendix.

Remark 5.2.6. Of course, there are many more types of bifurcation that can occur in a discrete-time dynamical system. However, since these five archetypes are sufficient to describe all transitions in our numerical bifurcation diagram, we decided to limit the definitions in this thesis to these five relevant bifurcation types.

6. Introducing stochasticity into the model

So far, the simulations and analysis of the model have been purely deterministic - we assumed constant parameter values during a single simulation. In particular, we assumed the same exact amount of summer every year for a long time. In real life, this assumption is not very realistic, as especially the summer length will be subject to quite some fluctuations.

In reality, most likely not only the summer length would vary over a long-term scale, but also other parameters. This variation in parameters might itself again be linked to summer length in some way - for example, species may adapt to longer summers through changes in their reproductive strategies, such as altered birth or death rates, as life-history traits are known to respond to environmental pressures [31]. Nevertheless, in the following we restrict ourselves to stochastic changes in the summer lengths a_S only, as those are most easily measurable in real life. While we will also explore different values of ν across simulations, we assume that each simulation is run with a fixed value of this parameter, reflecting the assumption that it remains constant under natural conditions during the considered time span.

The goal of the following simulations is to investigate what impact stochastic fluctuations in summer length have on the long-term behavior of our system. Which long-term behavior from the deterministic bifurcation diagram (Figure 5.1) is still present, and which behavior disappears? To compare the results to the purely deterministic ones, we aim for a two-dimensional diagram as before, capturing the long-term behavior for stochastically changing summer lengths. In the following, we first give the idea of how we want to implement stochastic changes in summer length and then introduce a new way of capturing long-term behavior.[1]

6.1. Idea for the simulation with stochastic summer lengths

In reality, summer length varies from year to year. To mimic this, we introduce stochasticity in our simulations by selecting a new value for a_S uniformly at random from $[a_{S_0} - \delta_{a_S}, a_{S_0} + \delta_{a_S}] =: I_{a_S}$ each year at the same time (i.e., right at the Poincaré sec-

[1] The classification algorithm from Chapter 4.1 can no longer be applied to these fuzzy simulation data, as both the classification as a cycle and the distinction between chaos and quasiperiodic orbits via FTLE no longer make sense. We will discuss this in more detail later in this Chapter.

tion), see Figure 6.1. Here, a_{S_0} corresponds to the base-summer length, i.e. the value of the parameter a_S for which we start the first year of the simulations.[2] The parameter $\delta_{a_S} \geq 0$ specifies the maximal deviation of the yearly summer length from its base value.

Remark 6.1.1. In practice, the parameter δ_{a_S} can be directly related to another quantity, δ which denotes the difference between the maximal and minimal summer lengths measured in days. We will use this notation frequently in the following. One can translate δ into δ_{a_S} for the interval of stochastic summer lengths I_{a_S} by setting $\delta_{a_S} = \frac{\delta}{365}$, so that

$$I_{a_S} = [a_{S_0} - \delta_{a_S}, a_{S_0} + \delta_{a_S}] = 2\left[T_{S_0} - \frac{\delta_{a_S}}{2}, T_{S_0} + \frac{\delta_{a_S}}{2}\right] =: 2I_{T_S},$$

and the length of this interval I_{T_S} is exactly the wiggleroom expressed as a fraction of days per year:

$$\left(T_{S_0} + \frac{\delta_{a_S}}{2}\right) - \left(T_{S_0} - \frac{\delta_{a_S}}{2}\right) = \delta_{a_S} = \frac{\delta}{365}.$$

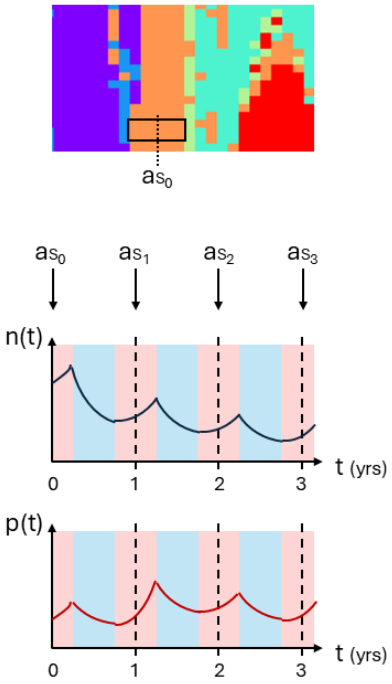

Figure 6.1.: Idea for stochastic summer length simulation. A new value of $a_S \in I_{a_S}$ is chosen every year at the same time, that is, right at the Poincaré section.

As initial conditions, we choose the long-term stationary results obtained when calculating the deterministic 2D numerical bifurcation diagram (Figure 5.1), c.f. Figure 4.3 for

[2] Note that to ensure realistic parameter values for a_{S_i}, we always assume that $a_{S_i} \in I_{a_S} \cap [0, 2]$.

examples. By restricting ourselves to these initial points, we implicitly assume that the system has been running for a long time with approximately the same parameter values and therefore has converged (close) to this long-term attractor. Thus, there is no need to start with an initial grid from scratch again.

For example, if the long-term attracting behavior for a_{S_0} is a 5-cycle in the deterministic results, we now compute 5 trajectories. If there are a lot of points in the deterministic results for the long-term attractor (chaos or quasiperiodic orbits [3]), we limit the number of trajectories in our simulation to $N = 500$ to keep the computational resources reasonable.[4]

All of those N points in the (n, p) phase space, calculated deterministically for a certain ν and our base summer length a_{S_0}, serve as initial conditions for one trajectory in our stochastic a_S simulations. After running with a_{S_0} for one year, we choose a new a_S within our interval $I_{a_S} = [a_{S_0} - \delta_{a_S}, a_{S_0} + \delta_{a_S}]$ starting from the end points of the previous simulation. We end up at some new points after one year and using those points as new initial conditions, we choose another $a_S \in I_{a_S}$ and do the same on and on. Note that we assume the same sequence of summer lengths $(a_{S_0}, a_{S_1}, a_{S_2}, \dots)$ for every trajectory.

We let the simulation run for $T_{end} = 500$ years and end up with N trajectories. After applying the Poincaré map to those trajectories, we plot the resulting points in the (n, p) phase space as in our deterministic simulations. However, if we start at a 5-cycle, the system will no longer end up at 5 distinct points in our Poincaré map, but rather 5 fuzzy islands. In general, we expect the inclusion of randomness in a_S to cause distortion of our long-term results.

The main objective is to investigate which qualitative behaviors are still visible and recognizable and which disappear. Applying the clustering algorithm is no longer promising, because on the one hand we do not have clearly repeating dynamics (periodic cycles) anymore - thus, making the detection of cycles difficult. On the other hand, we can also not apply the FTLE calculation anymore as we did before, as the parameter values change every year. Thus, there is a need for a new way of distinguishing between different qualitative behaviors among fuzzy point clouds. We came up with the following novel grid-based classification method.

[3] We always look at the last 50 points in the Poincaré map for each trajectory. For a 10×10 initial condition grid, this can lead to maximally 5000 points in our numerically obtained long-term attracting behavior. In particular, if we have a periodic orbit, many trajectories converge to this attractor, resulting in a smaller number of distinct points in the long-term Poincaré section. In contrast, for chaotic or quasiperiodic attractors, we have a larger number of points in the long-term Poincaré section.

[4] In case of coexistence of periodic orbits and non-periodic orbits (chaos, quasiperiodic orbits), the points belonging to the periodic orbits are always chosen to be among those 500 points. This might introduce some kind of bias, but as those cycles are an integral part of our system, we chose to prioritize them. However, the number 500 allows for using a large amount of points belonging to non-periodic orbits as initial conditions as well.

6.2. Grid-based classification method

Considering the trajectories as point clouds in the Poincaré sections, a natural approach is to analyze their scatter and whether they repeatedly visit specific locations, i.e., whether they concentrate in small regions of the predator-prey phase space. In order to do this, we first create a $N_n \times N_p$ grid in the (n, p) phase space.[5] Setting up a $N_n \times N_p$ matrix M allows counting the total number of times that any of the trajectories visit the corresponding grid cell. If we denote the number of points in grid cell (k, l), where the first component corresponds to the prey density and the second one to the predator density, by $m_{k,l}$, we have

$$\sum_{k=1}^{N_n} \sum_{l=1}^{N_p} m_{k,l} = N \cdot T_{end} \tag{6.1}$$

points to distribute in our matrix according to their locations.

As the number of trajectories depends on the deterministically obtained long-term dynamics and, as described before, is not constant over all combinations of ν and a_{S_0} (5 initial points in a 5-cycle versus 500 for chaos), we want to normalize the matrix by the number of trajectories, N, to allow better comparability between the different simulations. Thus, we get the normalized matrix

$$\bar{M} = \frac{1}{N} M \tag{6.2}$$

and

$$\sum_{k=1}^{N_n} \sum_{l=1}^{N_p} \bar{m}_{k,l} = T_{end}, \tag{6.3}$$

which is constant (and equal) for all the simulations we conduct to obtain our two-dimensional map in the (a_{S_0}, ν) space.

The next step is to use this matrix of the average number of visits per trajectory and count the number of empty grid cells. Furthermore, counting the number of grid cells $\bar{m}_{k,l}$ that have $0 < \bar{m}_{k,l} \leq 1$ entries, the ones that have $1 < \bar{m}_{k,l} \leq 2$ entries, etc. allows one to create a histogram. The histogram depicts the number (resp. fraction) of grid cells that are visited $(n, n+1]$ times per trajectory, where $n \in \mathbb{N}$. See Figure 6.2 for an example.

[5] The resolution of this grid can indeed impact the results quite a lot. By choosing the grid too narrow, we might not really recognize recurrence, while choosing it too coarse might lead to losing some key features as well (for example, the case where multiple distinct areas of high concentration are located in one single grid cell). For all simulations in this thesis, we chose the grid resolution to be $N_n \times N_p = 50 \times 50$ within our prey-predator phase plane $(n, p) \in [0, 1] \times [0, 1]$.

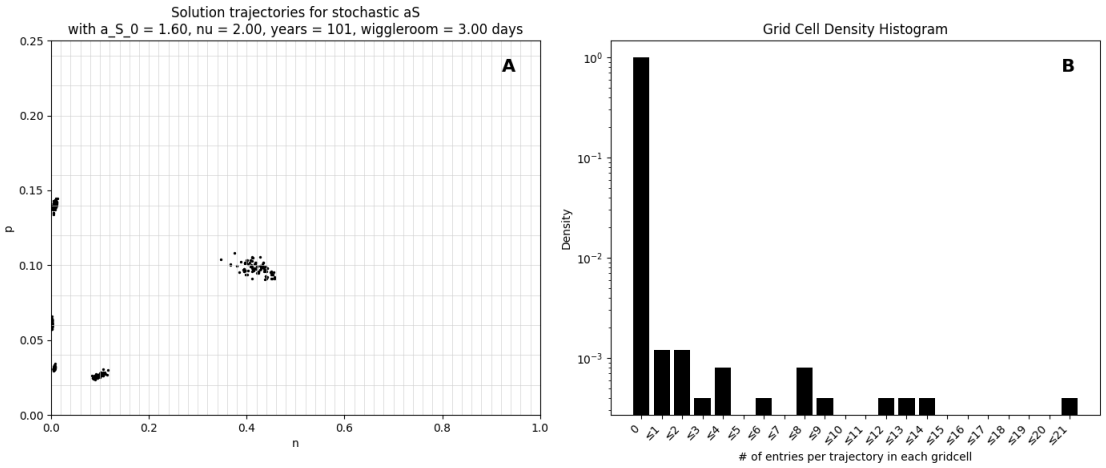

Figure 6.2.: Simulation of trajectories with stochastic summer lengths for $a_{S_0} = 1.6$ and $\nu = 2$ with a wiggleroom of $\delta = 3$ days run for 101 years. A: Poincaré map of the 5 solution trajectories, additionally the grid ($N_n \times N_p = 50 \times 50$ in $(n, p) \in [0, 1] \times [0, 1]$) is plotted. B: Histogram to the trajectory data for the corresponding grid in A. Note that the y-axis is logarithmic, so that even small values can be seen properly.

To give an example, when there is a distorted 5-year cycle (i.e. it appears as 5 islands in the prey-predator phase space), we expect a very small number of nonzero grid cells and those that indeed get visited to be visited often. Graphically speaking, there is a sharp descent in the histogram after the first category of zero-visit grid cells and a long tail to a few high-number-of-visits grid cells (see Figure 6.2 for example). On the other hand, a distorted quasiperiodic orbit or chaotic orbit is expected to fill a bigger chunk of the phase space, with most grid cells not being visited a lot of times. So, the histogram will look not as sharp, and the tail will be much shorter (i.e. no high-number-of-times visited grid cells indicating periodicity).

Given a histogram, the natural next step is to use some simple statistics, such as variance, mean, standard deviation, skewness, and kurtosis, to quantify these differences in the structure of the histogram. Using these statistical moments alongside the nonzero grid cell density allows one to compare the results of the stochastic simulations for different combinations of a_{S_0} and ν quantitatively. For a better comparability, the values of all the statistical moments are normalized by the corresponding maximum value across all simulations (all combinations of a_{S_0} and ν).

However, in order to qualitatively describe and interpret these differences, one needs to develop an approach for visualization. Looking at five archetypes of fuzzy simulation results (that is, five simulations for stochastic summer length, starting at qualitatively different behaviors in the corresponding deterministic simulations for a_{S_0} and ν, namely,

1-cycle, 5-cycle, quasiperiodic orbit, chaos and coexisting chaos and 5-cycle), collecting the statistics for each of them, and normalizing the values in each of the statistics, we can use these results to visualize the different properties for each archetype.

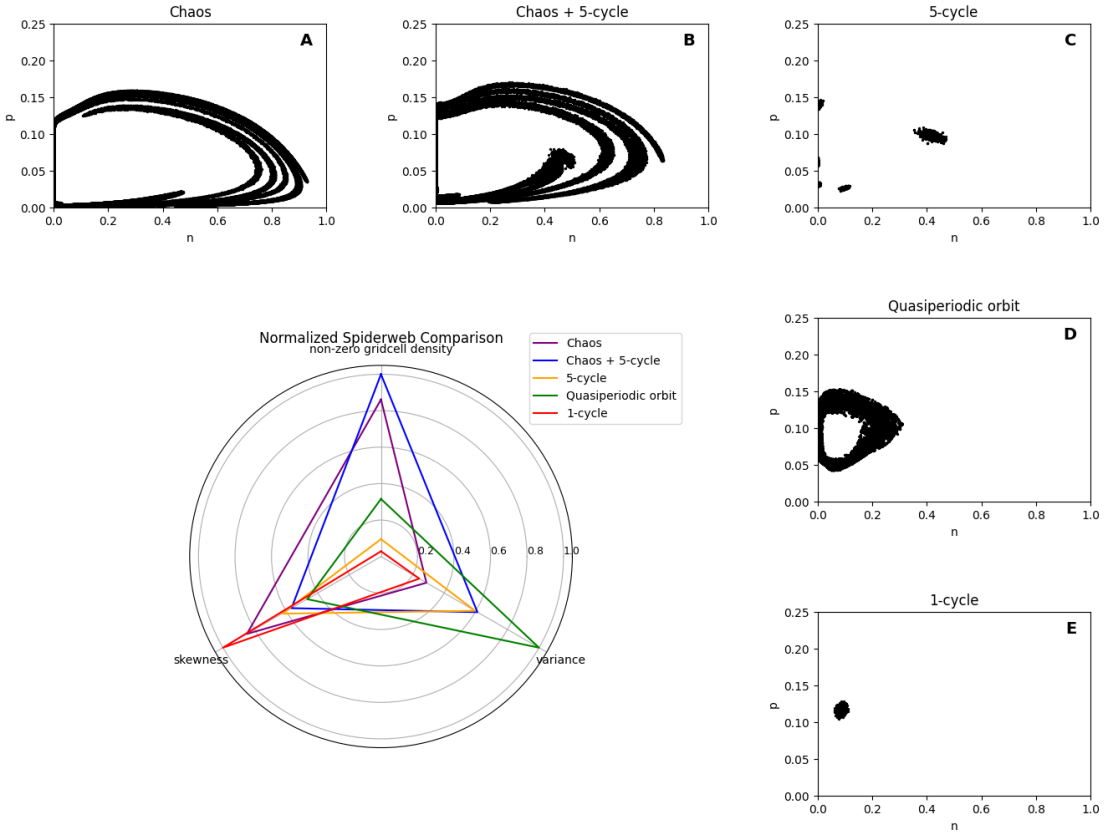

Figure 6.3.: Spiderweb graph and different archetypes of fuzzy behavior. The spiderweb graph depicts the profiles of each of the archetypes A-E w.r.t. nonzero grid cell density, variance and skewness (normalized by the respective maximum value across the five archetypes). Figures A-E: trajectory data in the Poincaré map of the simulation with stochastic summer lengths for different initial behavior (5 archetypes). All simulations for $\nu = 2$, 101 years and a wiggleroom $\delta = 3$ days. A: Chaos - $a_{S_0} = 1.3$, B: Chaos coexisting with 5-cycle - $a_{S_0} = 1.5$, C: 5-cycle - $a_{S_0} = 1.6$, D: Quasiperiodic orbit - $a_{S_0} = 1.7$, E: 1-cycle - $a_{S_0} = 1.8$.

In a spiderweb plot, different properties (in our case the different statistical moments and the nonzero grid cell density) are plotted on one axis each and thus allow one to visualize different behaviors. In our case, by just using a few simple statistics, the different qualitative behaviors of the five archetypes can be clearly distinguished. As Figure 6.3 shows, well-chosen combinations of two statistical moments and the nonzero grid cell

density already allow for a clear distinction of the different profiles in the spiderweb plot.[6]

When using only three different features, one can map the values in these three features directly to one of the three colors in the RGB-coloring scheme. Therefore, for a certain combination of a_{S_0} and ν, where we have calculated the statistics from the histogram and normalized the values across all combinations of a_{S_0} and ν, we get a certain RGB color from those normalized values. We can then create a grid in the (a_{S_0}, ν) space and color each point according to those RGB values. Areas of similar color on the map then correspond to similar values in the statistical moments and thus a similar behavior. This allows us to compare the results to the ones obtained in purely deterministic simulations.

6.3. Investigation of the impact of stochastic wiggleroom

We want to use the grid-based classification method to investigate how much impact stochastic summer lengths, and in particular the width of stochastic wiggleroom δ, have on the long-term dynamics of the system. For this, we perform simulations for different lengths of wiggleroom $\delta \in \{0, 3, 7, 10, 14\}$ days, create a diagram in the (a_{S_0}, ν) space, colored according to the RGB-colors defined by three statistical properties, and compare the diagrams with each other.

As mentioned in the description of the grid-based classification method in Chapter 6.2, there are different ways to choose the three properties for the RGB-coloring. One can argue that including the nonzero grid cell density is obvious, as this clearly helps to distinguish if only a small part of the phase space gets filled (so the trajectories concentrate only on a few spots, indicating a cycle) or a bigger chunk (indicating chaos or quasiperiodic orbit as they spread wider). For the remaining two properties, we considered the different combinations and chose the ones that worked best in terms of clearly different profiles of the five archetypes in the spiderweb diagram. The idea behind this is that if those five clearly different behaviors of scattered trajectories in the Poincaré maps have different profiles, they also have different colors in the 2D diagram, leading to a good distinction of different behaviors.

By investigating the different combinations, we saw that choosing the variance or the standard deviation for the second property, and the skewness or kurtosis (i.e. a higher statistical moment) for the third property yield the most distinctive profiles of the five archetypes. Therefore, all plots in the following were chosen to be colored by nonzero grid cell density, variance, and skewness.[7]

[6] Determining which of the statistics to use remains a challenge, but for our simulation results using the variance as well as kurtosis or skewness showed the best results in terms of clear distinction of different areas of behavior.

[7] Other combinations like variance and kurtosis, standard deviation and skewness or standard deviation and kurtosis showed similar behavior.

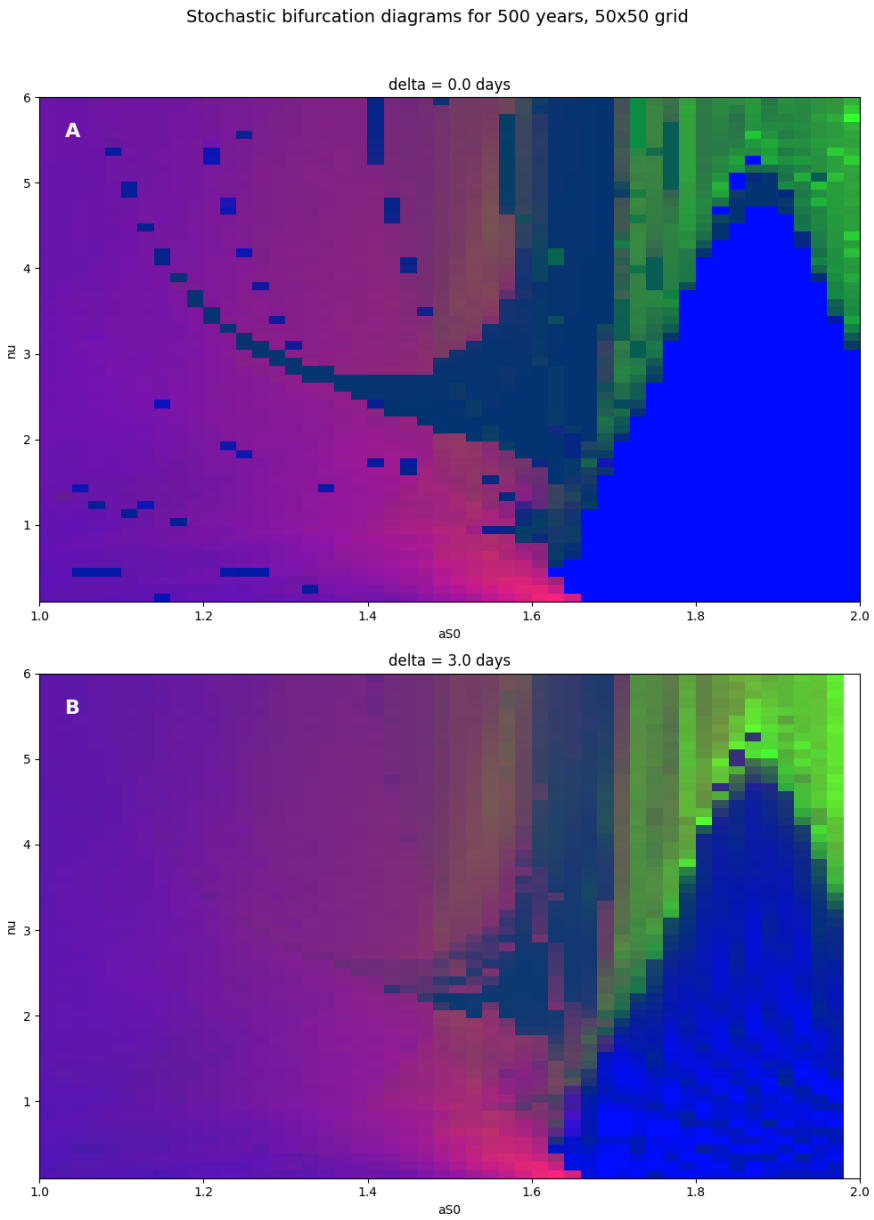

Figure 6.4.: Comparison of purely deterministic results with stochastic results. A: no stochastic wiggleroom ($\delta = 0$ days), i.e. purely deterministic results. B: including a stochastic wiggleroom of $\delta = 3$ days.

Figure 6.4 shows the comparison of the purely deterministic result (no wiggleroom, that is, $\delta = 0$ days) with the one with stochastic summer lengths for a wiggleroom

of $\delta = 3$ days.[8] For the case of no wiggleroom (Figure 6.4 A), we just started the simulations at the long-term attracting behavior obtained for the numerical bifurcation diagram (Figure 5.1), let it run for 500 years and then applied the grid-based classification method. This allows one to apply the new coloring method and thereby compare this purely deterministic result to the one where we actually do include stochastic changes in summer length.

Already for a small wiggleroom of $\delta = 3$ days (see Figure 6.4 B) a lot of properties get lost in the diagram. For example, in Figure 6.4 A, the small strands where the period doubling of the base 6 cycle occurs and interrupts the large area of chaotic behavior can be seen very sharply. Indeed, all the areas where the values in the Poincaré section concentrate on only a few points are shown in a blue shade and can be clearly distinguished from the other behavior. When allowing for small stochastic changes however, we see that these strands of the base 6 period-doubling get completely lost in Figure 6.4 B. Ecologically speaking, this means that in real life, where the summer lengths will always be subject to at least very small stochastic fluctuations, those 6-periodic (or subsequent 12- or 24- periodic) orbits are very unlikely to be measured.

However, the other key features, like the chaos, periodic orbits (now featured as scattered islands in the Poincaré map - see Figure 6.3 C and E), and quasiperiodic orbits still persist and can be distinguished very clearly.

The impact of the length of stochastic wiggleroom can be seen in Figure 6.5. It shows four Figures with different values of δ (A: $\delta = 3$ days, B: $\delta = 7$ days, C: $\delta = 10$ days and D: $\delta = 14$ days). One key feature that is resilient over all lengths of wiggleroom is the clear border between chaos and the 1-cycle for low values of ν around $a_{S_0} \approx 1.65$ (which corresponds to the area of a boundary crisis bifurcation in the deterministic bifurcation diagram). Stochastic summer lengths do not seem to have a large impact on this sharp distinction.

The area of the former 5-cycle is also still visible, but the distinction to bordering chaos or quasiperiodicity gets more difficult - the borders blur out. The area of quasiperiodic orbits for high values of ν and a_{S_0} expands drastically to the area where only a 1-cycle occurred in the deterministic results (high a_{S_0}, low ν). This means that for intermediate ν and larger wiggleroom δ, the trajectories from the initial 1-cycles show up as scattered trajectories in the Poincaré map and therefore can no longer be clearly distinguished from the Poincaré maps stemming from a quasiperiodic orbit as initial conditions.

[8] Note, that in Figure 6.4 B, at $a_{S_0} = 2$ there is only a white line. This corresponds to the limitations in wiggleroom: if we had a $\delta > 0$, this would lead to impossible simulations with $a_S > 2$.

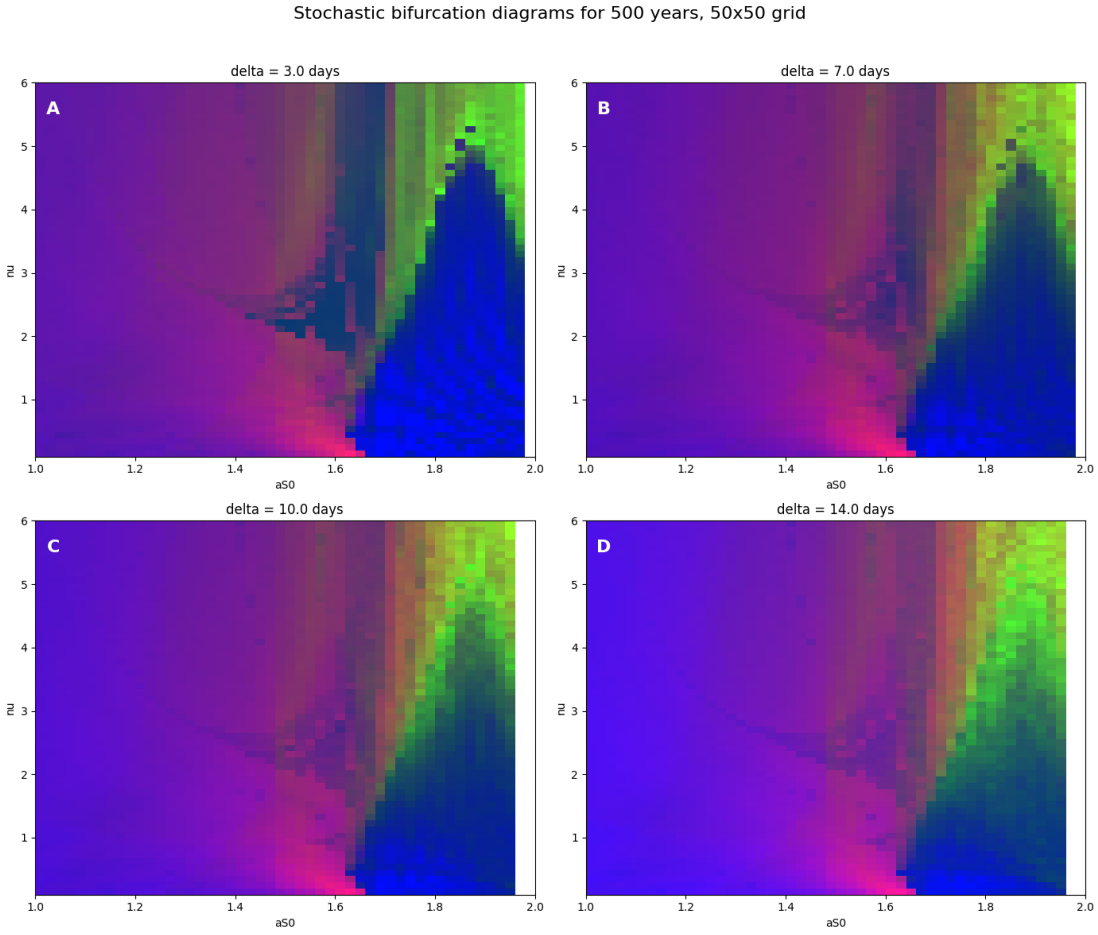

Figure 6.5.: Impact of different wiggleroom in stochastic summer lengths. All simulations are performed for 500 years and measured with a 50×50 grid. A: $\delta = 3$ days, B: $\delta = 7$ days, C: $\delta = 10$ days, D: $\delta = 14$ days.

7. Crossing boundaries in the bifurcation diagram - investigating transitions

When looking at bifurcations, and especially in the light of climate change, one thing of interest is how fast some transitions take place and whether they can be reversed in the same amount of time. In bifurcations that exhibit hysteresis (which includes saddle-node bifurcations for example), it is well known that the speed and direction of transitions can differ depending on whether the bifurcation parameter is increased or decreased. The reason behind it is that the system can end up in a different basin of attraction after the transition, making it hard or even impossible to return to the original state by just reversing the parameter [39]. Such bifurcations that exhibit hysteresis occur at so-called tipping points.

This theoretical behavior of hysteresis and irreversible transitions is not just abstract - it is observed in several key components of the Earth system. For example, the Greenland ice sheet may pass a critical temperature threshold beyond which melting becomes self-reinforcing and irreversible. Similarly, the Atlantic Meridional Overturning Circulation (AMOC) could collapse due to increased freshwater input, shifting the system into a new circulation regime that cannot be restored by simply reversing the forcing. Other examples include the potential dieback of the Amazon rainforest and the thawing of permafrost, both of which involve feedbacks that can push the system into fundamentally different states. These are all considered climate tipping points, and many of them are associated with saddle-node bifurcations and hysteresis behavior [4].

To uncover the impact of climate change on our system via changing summer lengths, we aim to investigate the speed of transitions when crossing boundaries in the 2D bifurcation diagram. Just like when introducing stochasticity into the system in Chapter 6, we again limit ourselves to changes in the summer length, that is, changes in a_S and assume ν to be fixed throughout a simulation. The goal is to investigate the transition across bifurcation boundaries in terms of speed of convergence to the new attracting structure, allowing a practical way of identifying changes that are difficult to reverse, or even irreversible.

7.1. Method description

In the following, we describe the approach for analyzing the speed of transition when crossing a bifurcation boundary. Just like the classification algorithm and the grid-based classification method, this is again a novel method. As before, we are only interested in the values of the trajectories at the Poincaré section. This will be sufficient information to determine (the speed of) convergence.

The idea is to start at one side of the bifurcation, namely at a_{S_0}.[1] Each of the N points in the long-term attracting structure of a_{S_0} serves as an initial condition for a trajectory. Again, like in Chapter 6, we implement a threshold for the initial conditions $N \leq 500$ to keep the necessary computational resources reasonable.

We then numerically calculate the solution, starting at these N initial conditions, but for the system at a_{S_1} instead of a_{S_0}. The value of this a_{S_1} is assumed to be constant throughout the simulation, so for all $\tau \in [0, \tau_{end}]$. a_{S_1} is assumed to be close to a_{S_0}, but on the other side of the bifurcation boundary under investigation. The solution trajectories themselves will then, of course, converge to the attracting structure for a_{S_1}. So, as in the stochastic summer length simulations, the deterministic long-term behavior obtained for calculating the 2D bifurcation diagram (Figure 5.1) plays an important role.

In order to measure convergence, the idea is as follows. For each trajectory, at each timestep (in the Poincaré map), we measure the minimum distance to the attracting structure for this a_{S_1}. As for the numerical bifurcation diagram, only the last 50 points in the Poincaré map for each trajectory were used, so the long-term attracting structure consists of at most 5000 points (as there were 100 trajectories initially).[2] Therefore, the minimum distance to the attracting structure is the minimum of the euclidean distances to these points.

By computing this minimum distance at every timestep (every year), one obtains the trajectory's minimum distance to the attracting structure as a function of time. Since the summer length (or rather a_{S_1}) is constant during the simulation, this graph is expected to follow an exponential decay. To quantify the speed of convergence, we model the decay as

$$d(\tau) = d_0 e^{-\lambda \tau} \tag{7.1}$$

We define the $100 \cdot p\%$ convergence time as the time until the minimum distance has decreased to $p \cdot 100\%$ of its initial value. Using this definition, the exponential decay

[1] Note, that ν is assumed to be constant throughout the whole simulation - i.e. the transitions only take place horizontally in the bifurcation diagram.

[2] This leads to some numerical limitations, especially in the case where the attracting structure is chaotic. However, it is still sufficient to get a sense of convergence, as we shall see.

rate λ can be estimated as

$$d(\tau_p) = p \cdot d_0 = d_0 e^{-\lambda \tau_p} \Rightarrow \lambda = \frac{-\ln(p)}{\tau_p}. \tag{7.2}$$

The parameter λ measures how fast the solutions converge to the new attracting structure and, therefore, how quickly a transition towards this new type of qualitative behavior takes place. A higher value of λ means faster exponential decay, and thus faster convergence.

However, this result might be (heavily) dependent on the initial condition for this trajectory. But one can take this approach one step further by averaging the minimal distance to the closest point on the attracting structure over all trajectories for each year resp. timestep. Then we end up with a time series of the averaged minimal distance towards the attracting structure over time. Just as before, one can then take this time series (assuming it now resembles a fairly smooth exponential decay) to calculate the coefficient for the speed of convergence, λ. The formulas (7.1) and (7.2) can be applied directly, assuming that $d(\tau)$ stands for the average minimal distance towards the attracting structure at time τ.

Remark 7.1.1. A crucial assumption for this method is that the data exhibit a smooth exponential decay in average minimal distance. If the curve is not always monotone decreasing (in particular, if there is some periodic noise in the exponential decrease - see Figure 7.2 for example), this estimate loses precision.

Another option to obtain some sense of the speed of convergence also relies on the average minimal distance to resemble an exponential decay. Instead of implementing a certain threshold p, one can use logarithmic scaling of the y-axis to fit a linear function to this resulting graph by the method of least squares. The decay of this linear function

$$y(\tau) = -\kappa\tau + y_0, \tag{7.3}$$

that is, the parameter κ, then serves as a new approximate for the speed of convergence. More precisely, by rescaling the linear approximation to the logarithmically transformed average minimal distance via an exponential function, one gets

$$\exp(y(\tau)) = \exp(-\kappa\tau + y_0) = e^{y_0} e^{-\kappa\tau} =: c e^{-\kappa\tau}, \tag{7.4}$$

and therefore κ serves as an approximate speed of convergence just like λ. In particular, in the simulation, both approaches - the one with the $p \cdot 100\%$ convergence time τ_p and the one with the least-squares fit - should give similar estimates for the speed of convergence.

7.2. Results

For defining the bifurcation types in Chapter 5.2, it did not matter where exactly in the (a_S, ν) space the transition takes place between two distinct areas, as long as they are not interrupted by a different area of behavior (and thus another bifurcation). We were just interested in the type of bifurcation and not, for example, in the exact values of the eigenvalues of the Jacobian when obtaining the stability loss of a cycle.

Now, however, we are interested in the speed of convergence, and here it indeed makes a difference where in the bifurcation diagram we cross a bifurcation boundary. Take, for example, the transition between a 1-cycle and a quasiperiodic orbit. As we simulated the 2D bifurcation diagram for discrete steps of a_S and ν, we only know that the 'real' location of the bifurcation is between two such simulations, where for one a_{S_0} we have a 1-cycle and for the other $a_{S_1} = a_{S_0} - \varepsilon$ we have a quasiperiodic orbit. In fact, the exact place for this bifurcation can lie anywhere in $[a_{S_0} - \varepsilon, a_{S_0}]$. If now, for a certain ν_0, this 'real' location would be right after $a_{S_0} - \varepsilon$, that could lead to the quasiperiodic orbit being already quite large in size at a_{S_0}. On the other hand, for a ν_1 slightly different than ν_0, where the 'real' location would be just before a_{S_0}, the quasiperiodic orbit at a_{S_0} would be rather small.

This could lead to the fact that in the first case, the transition could take longer (as it needs to converge to an attractor further away) as in the second one (where the initial condition of the 1-cycle is already close to the small quasipieriodic orbit). However, as the $p \cdot 100\%$ convergence time already takes the initial average distance into account, we argue that the convergence times are still approximately equal for nearby regions along one boundary, as long as we cross the boundary in the same direction. Therefore, in the following analysis, we only limit ourselves to a few handpicked transitions.

For example, assume $\nu = 2.8$, $a_{S_0} = 1.78$ (so, starting at a 1-cycle) and $a_{S_1} = 1.76$ (convergence to a quasiperiodic orbit). In Figure 7.1 the numerically obtained trajectory, starting from the location of the 1-cycle, is shown for different times. One can see that this single trajectory indeed converges to the new attractor (the quasiperiodic orbit) after some time. This convergence can be measured using the minimum distance from that trajectory to the quasiperiodic orbit. In Figure 7.2 we see that the evolution of this minimum distance approximately resembles an exponential decay.

The two ways of measuring the convergence speed can be applied to these data. First, the time until the minimum distance from the attractor has reached 1% of its initial value, $t_{0.01}$, can be used to approximate the speed of exponential decay, λ, as in (7.2). The measurements show that $t_{0.01} = 517$ years, and therefore

$$\lambda = -\frac{\ln(0.01)}{517} \approx 0.0089.$$

This parameter λ is then used to approximate the exponential decay function, which is

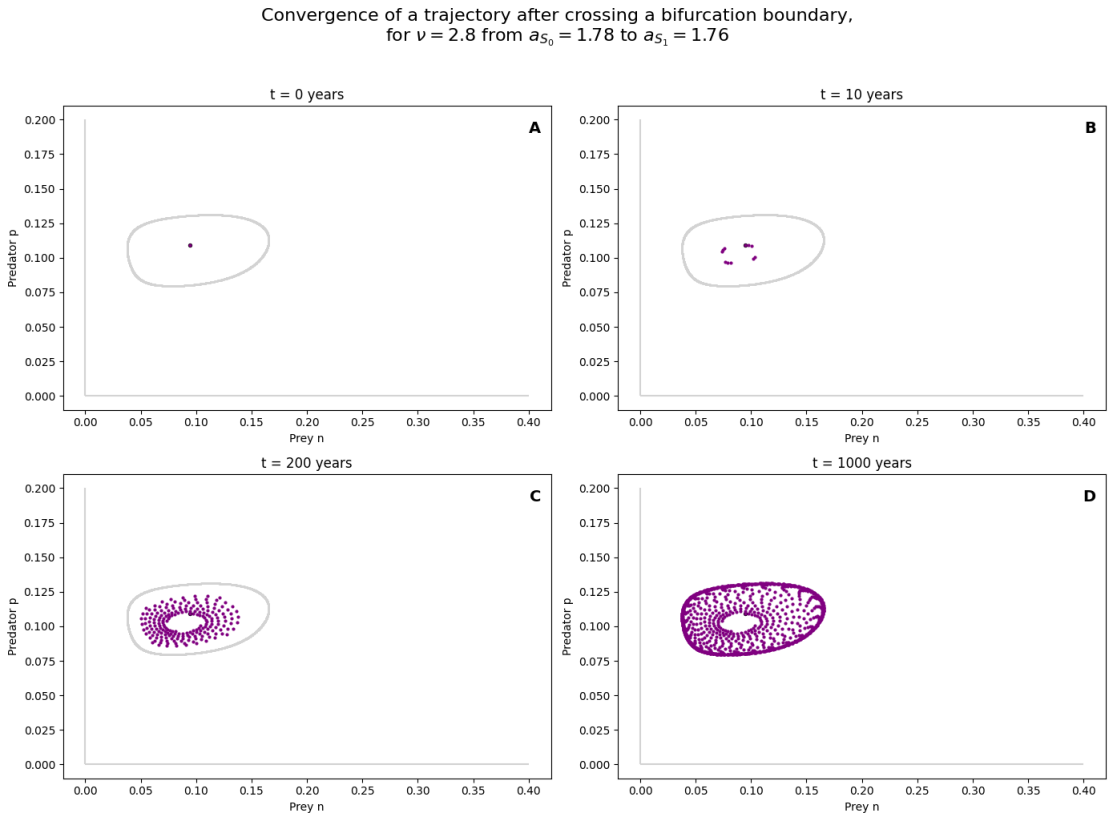

Figure 7.1.: Convergence of a trajectory after crossing a bifurcation boundary, for $\nu = 2.8$ from $a_{S_0} = 1.78$ (1-cycle) to $a_{S_1} = 1.76$ (quasiperiodic orbit). The attractor (quasiperiodic orbit) is plotted in light grey, the initial condition (1-cycle) in black and the evolution of the trajectory in the Poincaré map in purple. A: system at time $t = 0$, B: trajectory for the first 10 years, C: trajectory for the first 200 years, D: trajectory for the first 1000 years.

shown in blue in Figure 7.2. By construction, this fit is exact for the initial condition and seems to slightly underestimate the average minimal distance to the attractor for $t > 0$. However, it seems like a reasonably good fit.

Note that the value of the parameter λ does not mean much on its own. The interpretation of the 1% convergence time is much more meaningful in the context of speed of convergence, as it gives a good feeling of how fast this transition happens.

Remark 7.2.1. In a real-life scenario, or even already in numerical cases, where the location of the attractor is not fully known, or consists only of some N points, this method has its limitations. For example, consider a transition to a chaotic attractor with an already low initial average minimum distance. In the chaotic case, the trajectory

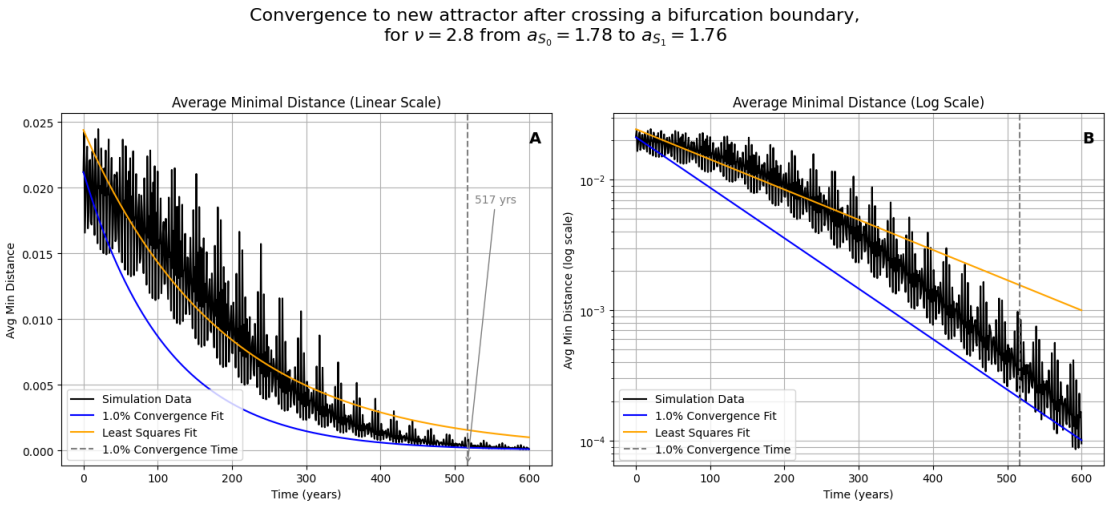

Figure 7.2.: Average minimal distance to attracting structure after crossing a boundary, for $\nu = 2.8$ from $a_{S_0} = 1.78$ (1-cycle) to $a_{S_1} = 1.76$ (quasiperiodic orbit). The average minimal distance is plotted in black. The estimated exponential decay functions are plotted in blue (fitted via the 1% convergence time) resp. orange (fitted via least-squares). A: simulated data and the estimators for exponential decay in linear scale. The 1% convergence time is $t_{0.01} = 517$ years. B: simulated data and the estimators for exponential decay in logarithmic scale.

never revisits the exact same locations. Moreover, the points in the chaotic folds can be scattered far apart. As a result, the average minimum distance may never, or only very slowly, decrease to 1% of the initial value. In such situations, the approximate exponential decay cannot be calculated; see Figure D.3 for an example.

The other way to fit an exponential decay function to the simulated data, namely by using the method of least squares, always works, as it is not dependent on any previously calculated numbers, but only on the data itself.[3] In Figure 7.2, this fit is shown as an orange curve and, although overestimating the average minimum distance in the beginning, approximates the decay quite well for intermediate times. Especially in the logarithmically scaled graph it can be seen that the two methods give similar estimators for the speed of convergence (as the slopes of the two functions are similar [4]).

The estimators for the speed of convergence of the two approaches are very similar. However, since the approach of fitting via least squares gives a slightly different (and

[3] However, note that this estimator depends on all the data in the simulation. In particular, this means that different simulation lengths could lead to different estimators for the speed of convergence κ.

[4] There is still a visible difference in slopes in this Figure. For other scenarios, such as in Figures 7.3 and 7.4, the slopes are even more similar.

in most cases lower) estimate for the speed of convergence ($\kappa \approx 0.0053$) than the fit via $p \cdot 100\%$ convergence levels (as the slope of the blue curve is steeper than that of the orange curve), it is of interest to check if this difference is always approximately the same.

To investigate this, we assume a linear connection between λ and κ, in particular, that

$$\kappa \approx k\lambda. \tag{7.5}$$

If $k \approx 1$, then the two estimators are similar to each other and thus give approximately the same function for the exponential decay in the average minimum distance.

In Table 7.1, the estimators for κ and λ were calculated for different scenarios of crossing a bifurcation boundary. The value of k is then calculated by dividing κ by λ. We see that for many of the simulations, this value appears to be approximately $k \approx 0.7$. For a few simulations, namely 7, 11 and 12, $k \approx 1$, so the estimators are very similar.

Nr.	ν	a_{S_0}	type 0	a_{S_1}	type 1	$t_{0.01}$	λ	κ	k
1	4.1	1.7	5-cycle	1.74	Q	34	0.1354	0.0931	0.688
2	4.1	1.74	Q	1.7	5-cycle	140	0.0329	0.0224	0.681
3	3.0	1.68	5-cycle	1.7	5-cycle + Q	82	0.0562	0.0401	0.714
4	3.0	1.7	5-cycle + Q	1.68	5-cycle	83	0.0555	0.0382	0.688
5	3.1	1.52	chaos	1.58	20-cycle	235	0.0196	0.0294	1.5
6	4.0	1.82	1-cycle	1.8	Q	369	0.0125	0.0049	0.392
7	4.0	1.8	Q	1.82	1-cycle	338	0.0136	0.013	0.956
8	0.2	1.62	chaos	1.66	1-cycle	142	0.0324	0.0237	0.731
9	0.2	1.66	1-cycle	1.62	chaos	103	0.0447	0.0091	0.204
10	2.8	1.78	1-cycle	1.76	Q	517	0.0089	0.0053	0.596
11	2.8	1.76	Q	1.78	1-cycle	327	0.0141	0.0152	1.08
12	5.2	1.7	5-cycle	1.74	Q	49	0.094	0.088	0.936
13	5.2	1.74	Q	1.7	5-cycle	97	0.0475	0.029	0.611

Table 7.1.: Comparison of exponential decay parameters. 13 different simulations for crossing a bifurcation boundary from type 0 at a_{S_0} to type 1 at a_{S_1} are shown. Q stands for 'quasiperiodic orbit'. The unit of the 1% convergence time $t_{0.01}$ is years. Columns λ and κ show the respective values of the estimators for the speed of convergence and k is calculated from λ and κ by Equation (7.5).

The reason for k not being approximately 1 for every single simulation might lie in our approaches as well as in the smoothness of the data. For a detailed explanation see Appendix D. However, there is still strong evidence for a direct linear connection between λ and κ that requires further investigation.

As seen in Figures 7.2, 7.3 and 7.4, both ways of estimating the exponential decay give fairly good fits to the data and thus serve as reliable estimators for the speed of

convergence. Therefore, in cases where the method of $p \cdot 100\%$ convergence levels does not apply, the speed of convergence can still be estimated by the fit via least squares (by assuming $\kappa \approx k\lambda$), and then transformed into an estimator for the $p \cdot 100\%$ convergence time as follows:

$$t_p \approx -\frac{k \ln(p)}{\kappa}. \tag{7.6}$$

This allows for an intuitive interpretation of the speed of convergence that provides much more qualitative information than just the number κ.

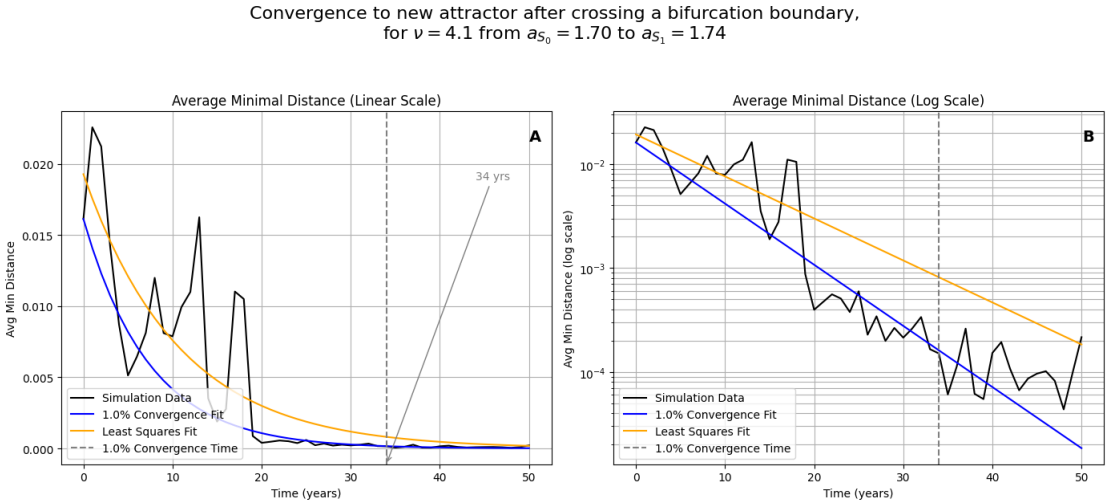

Figure 7.3.: Average minimal distance to attracting structure after crossing a boundary, for $\nu = 4.1$ from $a_{S_0} = 1.70$ (5-cycle) to $a_{S_1} = 1.74$ (quasiperiodic orbit). The average minimal distance is plotted in black. The estimated exponential decay functions are plotted in blue (fitted via the 1% convergence time) resp. orange (fitted via least-squares). A: simulated data and the estimators for exponential decay in linear scale. The 1% convergence time is $t_{0.01} = 34$ years. B: simulated data and the estimators for exponential decay in logarithmic scale.

As a second example, we want to focus on differences in the speed of convergence when moving across the bifurcation boundary in both directions. Consider the transitions between a 5-cycle and a quasiperiodic orbit for $\nu = 4.1$. First, assume that the simulation starts at the locations of the 5-cycle obtained for $a_{S_0} = 1.7$, and is conducted for $a_{S_1} = 1.74$ (where the attractor is a quasiperiodic orbit). The minimum average distance converges to the new attractor very rapidly (see Figure 7.3) - it only takes 34 years until 1% of the average minimum distance is reached. This means that by increasing the summer length across this bifurcation boundary, the stable 5-periodic behavior changes very quickly to a quasiperiodic behavior.

In contrast, when switching a_{S_0} and a_{S_1}, that is, now moving from a quasiperiodic

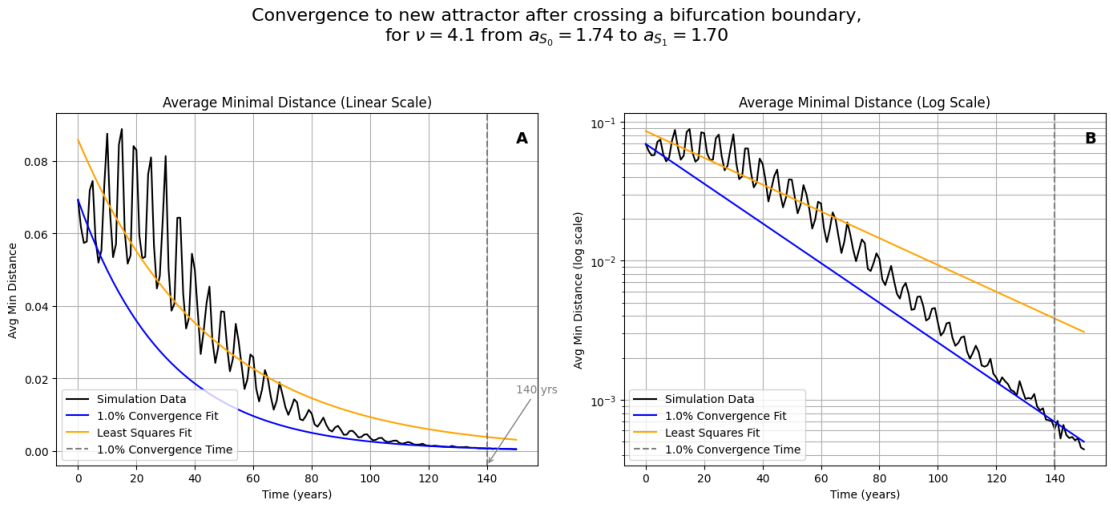

Figure 7.4.: Average minimal distance to attracting structure after crossing a boundary, for $\nu = 4.1$ from $a_{S_0} = 1.74$ (quasiperiodic orbit) to $a_{S_1} = 1.70$ (5-cycle). The average minimal distance is plotted in black. The estimated exponential decay functions are plotted in blue (fitted via the 1% convergence time) resp. orange (fitted via least-squares). A: simulated data and the estimators for exponential decay in linear scale. The 1% convergence time is $t_{0.01} = 140$ years. B: simulated data and the estimators for exponential decay in logarithmic scale.

orbit to a 5-cycle, the trajectories converge much slower (see Figure 7.4). The average minimum distance reaches 1% of its initial value after 140 years, which amounts to a large discrepancy compared to the 34 years observed before.

In practice, this difference can be interpreted as a tipping point. Increasing summer lengths induce a fast transition from a 5-cycle to a quasiperiodic orbit. However, if one wants to return to the original system (for example, if efforts to counteract climate change lead to reducing the summer length again), this might take way longer.

Such a mismatch in convergence times also occurs in other transitions, however not as extreme as in this case between a quasiperiodic orbit and a 5-cycle.[5] The reason for this exact mismatch remains unclear and calls for further investigation.

In general, transitions from quasiperiodic orbits or chaos towards cyclic behavior show a very smooth exponential decay in the average minimal distance towards the attractor. This stems from the fact that there are many trajectories, and so normalizing over all of them cancels out extreme outliers.

Transitioning from cycles towards non-cyclic behavior, we do not see a strict decline, but

[5] See Table 7.1 for convergence times for different transitions.

rather some periodic variation to a (generally still exponential) decay. This periodic noise typically occurs with the same period of the cycle for which the simulation started with. However, the exact reason for this periodic noise showing up in the average minimal distance is unclear, highlighting the need for further investigation in the future.

8. Discussion

The model developed in this thesis builds upon the framework of Tyson and Lutscher [42], extending it to allow for a more realistic and mathematically tractable representation of seasonal predator-prey dynamics. By introducing a smooth seasonal switching function, we were able to preserve the biological realism of distinct seasonal phases while maintaining a continuous right-hand side, which ensures that standard methods of dynamical systems theory, such as bifurcation analysis and Finite-Time Lyapunov exponents, can be applied in a straightforward manner. In contrast, a discontinuous formulation would place the system outside the scope of these classical approaches and instead require the use of specialized techniques for nonsmooth dynamics. This approach balances biological realism with mathematical tractability, allowing exploration of complex dynamics.

The classification algorithm developed in Chapter 4.1 proved to be a powerful tool for identifying and distinguishing between periodic, quasiperiodic, and chaotic long-term behaviors [32]. It allows for handling coexisting attractors by simulating a grid of initial trajectories to ensure that all long-term dynamics are captured. By applying a clustering algorithm to a weighted graph constructed from trajectory similarities, the method groups trajectories that are most similar over time. Subsequent computation of FTLE then provides a robust distinction between quasiperiodic orbits and chaos. While not all classifications are perfect due to the need for subjective, user-defined thresholds, the method provides a reliable way to automate the classification of all long-term attractors for a given parameter combination. The method is particularly valuable for higher-dimensional bifurcation diagrams and for systems with multiple coexisting attractors. As such, it could be applied in other projects or scenarios where complex long-term behaviors need to be classified automatically.

The resulting bifurcation diagram in the (a_S, ν)-space revealed a rich variety of behaviors, including multiple types of bifurcations and transitions between different qualitative behaviors. Although the diagram provides a coarse numerical approximation, it successfully identifies the most important regions of distinct long-term behavior. Finer grids would increase resolution but at a significant computational cost. For the purposes of exploring general patterns and transitions, the current numerical approximation is sufficient.

One particularly interesting result was the apparent stabilizing effect of longer summers in certain regions of parameter space, especially in the presence of strong generalist predation. While this may seem counterintuitive given the common association of climate

change with ecological instability, it underlines the complexity of ecological systems and the importance of predator-prey interactions. Importantly, this finding should not be interpreted as suggesting that climate change is beneficial. On the contrary, our results emphasize that even small shifts in seasonal patterns can lead to abrupt and potentially irreversible changes in ecosystem dynamics. This reinforces the urgency of understanding and addressing the multifaceted impacts of climate change.

Introducing stochastic summer lengths further enhanced the realism of the simulations, reflecting natural year-to-year variability. This approach prevents strict periodicity from being determined, but the grid-based classification and RGB-coloring of the averaged Poincaré sections still allow us to distinguish between long-term behaviors in a visually intuitive way. Boundaries between behaviors are blurred into smooth gradients rather than discrete categories, but this is expected given the variability in summer lengths. Importantly, this also demonstrates that the method could potentially be applied to real ecological data, which are inherently noisy, providing a bridge between theoretical predictions and empirical observations.

The investigation of transition speeds across bifurcation boundaries revealed the presence of tipping points - parameter thresholds where transitions occur asymmetrically. Two approaches were used to quantify convergence speeds. The 1% convergence method is straightforward and easy to interpret but can fail when the attractor for the new parameter value is not fully captured, such as in chaotic regions with sparse sampling. Fitting an exponential decay via least-squares provides a more reliable estimate, assuming that the average distance to the new attractor generally follows an exponential decay. Each method has limitations, particularly regarding simulation duration and initial condition sampling, but combining them provides both interpretability and robustness. Identifying these tipping points is especially relevant in the context of climate-change-induced shifts in predator-prey dynamics, where small changes can trigger abrupt and potentially irreversible transitions.

Despite these insights, several limitations remain. The model does not include extinction thresholds, spatial structure, or migration, which could significantly influence dynamics in real ecosystems. Parameter estimates are based on limited field data, and more accurate measurements would improve ecological realism. While the classification algorithm and convergence analyses are robust, they rely on thresholds and finite computational resources. Finer grids or longer simulations could increase precision but at additional computational cost.

Overall, the combination of a tractable seasonal model, automated classification, stochastic simulations, and convergence analysis allows for a detailed and nuanced understanding of the system's dynamics. The methods developed here are broadly applicable and provide a strong foundation for future work, including extending bifurcation diagrams to higher dimensions, applying the approach to real ecological datasets, and refining the analysis of critical transitions.

9. Conclusion

In this thesis, we set out to answer the question: *How do changes in seasonal transitions affect the dynamics of small rodent populations in northern Fennoscandia?* Our results show that changes in summer length can substantially alter predator-prey dynamics, shifting populations between periodic, quasiperiodic, and chaotic regimes. Small stochastic fluctuations in season length blur fine-scale structures but do not fundamentally change the qualitative behavior of the system. Additionally, the speed of transitions across bifurcation boundaries depends on the direction of change, highlighting potential sensitivity in the system to climate-driven seasonal shifts.

Building on this, we developed and analyzed a seasonally structured predator-prey model that captures the distinct dynamics of summer and winter interactions. By smoothly connecting seasonal equations and applying a range of mathematical tools, we were able to explore the system's long-term behavior across a wide parameter space in a biologically meaningful and mathematically rigorous way.

A key contribution of this work is the implementation of a novel classification algorithm capable of distinguishing between periodic, quasiperiodic, and chaotic attractors, even in the presence of multiple coexisting behaviors. This algorithm enabled the construction of a detailed bifurcation diagram in the (a_S, ν)-space, revealing a rich landscape of dynamical regimes and bifurcation types. The identification of five distinct bifurcation mechanisms highlights the complexity of the system and its sensitivity to seasonal and ecological parameters.

We further extended our analysis to include stochastic seasonal variability, simulating more realistic ecological conditions. Although fine structures in the deterministic bifurcation diagram were sensitive to noise, the broader qualitative behaviors remained robust. To analyze these fuzzy attractors, we introduced a new grid-based classification method that, despite its limitations, proved effective in distinguishing between different types of long-term behavior in noisy systems. This method may also be applicable to real-world ecological data, which is often subject to similar variability.

Finally, we investigated the speed of transitions across bifurcation boundaries and identified tipping points - parameter thresholds where transitions in one direction occur significantly faster than in the reverse. These findings have important implications for understanding ecological resilience and the potential irreversibility of climate-induced changes.

Overall, this thesis contributes a flexible and extensible modeling framework for studying seasonally structured ecological systems. The tools and methods developed here provide a foundation for future research, including the incorporation of extinction thresholds, spatial dynamics, and more precise ecological data. In the context of ongoing climate change, understanding how seasonal shifts affect predator-prey interactions is not only mathematically interesting but also ecologically urgent.

Bibliography

[1] Henry D. I. Abarbanel. *Analysis of Observed Chaotic Data*. Springer, New York, 1996.

[2] Nikolas Olson Aksamit. Lecture notes on climate dynamics, 2024. Unpublished lecture notes, UiT - The Arctic University of Norway, 2024.

[3] Kathleen T Alligood, Tim D Sauer, James A Yorke, and David Chillingworth. Chaos: an introduction to dynamical systems. *SIAM Review*, 40(3):732–732, 1998.

[4] David I Armstrong McKay, Arie Staal, Jesse F Abrams, Ricarda Winkelmann, Boris Sakschewski, Sina Loriani, Ingo Fetzer, Sarah E Cornell, Johan Rockström, and Timothy M Lenton. Exceeding 1.5 c global warming could trigger multiple climate tipping points. *Science*, 377(6611):eabn7950, 2022.

[5] Dominique Berteaux, Gilles Gauthier, Florent Domine, Rolf A. Ims, Scott F. Lamoureux, Esther Lévesque, and Nigel Yoccoz. Effects of changing permafrost and snow conditions on tundra wildlife: Critical places and times. *Arctic Science*, 3(2):65–90, 2017.

[6] A. V. Bobretsov. *Population ecology of small mammals of flat and mountain landscapes of North-East of the European part of Russia*. Scientific publishing partnership KMK, 2016.

[7] Hendrik W Broer, George B Huitema, and Mikhail B Sevryuk. *Quasi-periodic motions in families of dynamical systems: order amidst chaos*. Springer, 1996.

[8] Terry V. Callaghan, Margareta Johansson, Ross D. Brown, Pavel Ya. Groisman, Niklas Labba, Vladimir Radionov, Roger G. Barry, Olga N. Bulygina, Richard L. H. Essery, D. M. Frolov, Vladimir N. Golubev, Thomas C. Grenfell, Marina N. Petrushina, Vyacheslav N. Razuvaev, David A. Robinson, Peter Romanov, Drew Shindell, Andrey B. Shmakin, Sergey A. Sokratov, Stephen Warren, and Daquing Yang. The Changing Face of Arctic Snow Cover: A Synthesis of Observed and Projected Changes. *AMBIO*, 40(1):17–31, 2011.

[9] Konstantinos Efstathiou. Lecture 15: Dynamical systems and poincaré maps. https://www.efstathiou.gr/dku-math-303/lecture-15.pdf, 2023. Lecture notes, Department of Mathematics, University of Crete.

[10] Dorothée Ehrich, Niels M Schmidt, Gilles Gauthier, Ray Alisauskas, Anders Angerbjörn, Karin Clark, Frauke Ecke, Nina E Eide, Erik Framstad, Jay Frandsen, et al. Documenting lemming population change in the arctic: Can we detect trends? *Ambio*, 49:786–800, 2020.

[11] Alexandra Erbach, Frithjof Lutscher, and Gunog Seo. Bistability and limit cycles in generalist predator–prey dynamics. *Ecological Complexity*, 14:48–55, 2013.

[12] M. Fernández-Guasti. Squdel Function: Square Wave Approximation Without Ringing. *Circuits, Systems, and Signal Processing*, 38(2):764–773, 2019.

[13] Olivier Gilg, Ilkka Hanski, and Benoît Sittler. Cyclic Dynamics in a Simple Vertebrate Predator-Prey Community. *Science*, 302(5646):866–868, 2003.

[14] Alireza Hadjighasem, Daniel Karrasch, Hiroshi Teramoto, and George Haller. Spectral-clustering approach to lagrangian vortex detection. *Physical Review E*, 93(6):063107, 2016.

[15] George Haller. Lagrangian coherent structures. *Annual review of fluid mechanics*, 47(1):137–162, 2015.

[16] Ilkka Hanski, Lennart Hansson, and Heikki Henttonen. Specialist predators, generalist predators, and the microtine rodent cycle. *The Journal of Animal Ecology*, pages 353–367, 1991.

[17] Ilkka Hanski, Peter Turchin, Erkki Korpimäki, and Heikki Henttonen. Population oscillations of boreal rodents: regulation by mustelid predators leads to chaos. *Nature*, 364(6434):232–235, 1993.

[18] Lennart Hansson and Heikki Henttonen. Gradients in density variations of small rodents: The importance of latitude and snow cover. *Oecologia*, 67(3):394–402, 1985.

[19] John-André Henden, Rolf A Ims, and Nigel G Yoccoz. Nonstationary spatiotemporal small rodent dynamics: evidence from long-term norwegian fox bounty data. *Journal of Animal Ecology*, 78(3):636–645, 2009.

[20] Heikki Henttonen, Olivier Gilg, Rolf A Ims, Erkki Korpimäki, and Nigel G Yoccoz. Ilkka hanski and small mammals: from shrew metapopulations to vole and lemming cycles. In *Annales Zoologici Fennici*, volume 54, pages 153–162. BioOne, 2017.

[21] Heikki Henttonen, Tarja Oksanen, Aarre Jortikka, and Voitto Haukisalmi. How Much Do Weasels Shape Microtine Cycles in the Northern Fennoscandian taiga? *Oikos*, 50(3):353–365, 1987.

[22] Crawford S Holling. The components of predation as revealed by a study of

small-mammal predation of the european pine sawfly1. *The canadian entomologist*, 91(5):293–320, 1959.

[23] Rolf Anker Ims and Eva Fuglei. Trophic Interaction Cycles in Tundra Ecosystems and the Impact of Climate Change. *BioScience*, 55(4):311–322, 2005.

[24] Sonja Kivinen, Sirpa Rasmus, Kirsti Jylhä, and Mikko Laapas. Long-term climate trends and extreme events in northern fennoscandia (1914–2013). *Climate*, 5(1):16, 2017.

[25] Tero Klemola, Terje Pettersen, and Nils Chr. Stenseth. Trophic interactions in population cycles of voles and lemmings: A model-based synthesis. In *Advances in Ecological Research*, volume 33, pages 75–160. Elsevier, 2003.

[26] Charles J. Krebs, Rudy Boonstra, and Stan Boutin. Using experimentation to understand the 10-year snowshoe hare cycle in the boreal forest of North America. *Journal of Animal Ecology*, 87(1):87–100, 2018.

[27] Yuri A Kuznetsov. *Elements of applied bifurcation theory*. Springer, 1998.

[28] Shawn J Leroux, Maxim Larrivée, Véronique Boucher-Lalonde, Amy Hurford, Juan Zuloaga, Jeremy T Kerr, and Frithjof Lutscher. Mechanistic models for the spatial spread of species under climate change. *Ecological Applications*, 23(4):815–828, 2013.

[29] Mark A. Linnell, Clinton W. Epps, Eric D. Forsman, and William J. Zielinski. Survival and Predation of Weasels (Mustela erminea, Mustela frenata) in North America. *Northwest Science*, 91(1):15–26, 2017.

[30] Anna Luomaranta, Juha Aalto, and Kirsti Jylhä. Snow cover trends in finland over 1961–2014 based on gridded snow depth observations. *International Journal of Climatology*, 39(7):3147–3159, 2019.

[31] Oliver Manlik. The importance of reproduction for the conservation of slow-growing animal populations. In Pierre Comizzoli, Janine L. Brown, and William V. Holt, editors, *Reproductive Sciences in Animal Conservation*, volume 1200 of *Advances in Experimental Medicine and Biology*, pages 13–28. Springer Nature Switzerland, 2019.

[32] Julia Mikhailova, Clemens Breuß, Nikolas Aksamit, and Nigel Yoccoz. Changes in seasonality and dynamics of the rodent-mustelid system. Manuscript in press, 2025.

[33] Péter K Molnár, Andrew E Derocher, Gregory W Thiemann, and Mark A Lewis. Predicting survival, reproduction and abundance of polar bears under climate change. *Biological Conservation*, 143(7):1612–1622, 2010.

[34] Andrew Ng, Michael Jordan, and Yair Weiss. On spectral clustering: Analysis and an algorithm. *Advances in neural information processing systems*, 14, 2001.

[35] V. A. Orlov, D. A. Sarancha, and O. A. Shelepova. Matematicheskaya model dinamiki chislennosti lemmingov (lemmus, dicrostonyx) i ejo preminenie dlja opisanija populjazij zapadnogo tajmyra / mathematical model of the dynamics of the lemming population (lemmus, dicrostonyx) and its use to describe the populations of eastern taimyr. *Ecologiya*, 2:43–51, 1986.

[36] Ruy M. O. Pauletti and Edgard S. Almeida Neto. A finite-difference approximation to newton method's jacobian matrices. In *Mecánica Computacional*, volume XXIX, pages 2457–2474. AMCA, 2010.

[37] II Rypina, Michael G Brown, Francisco J Beron-Vera, Huseyin Koçak, Maria J Olascoaga, and IA Udovydchenkov. On the lagrangian dynamics of atmospheric zonal jets and the permeability of the stratospheric polar vortex. *Journal of the Atmospheric Sciences*, 64(10):3595–3610, 2007.

[38] Nils Chr. Stenseth and Rolf Anker Ims. *The Biology of Lemmings*. Academic Press, 1993.

[39] Steven H Strogatz. *Nonlinear dynamics and chaos: with applications to physics, biology, chemistry, and engineering*. Chapman and Hall/CRC, 2024.

[40] John Michael Tutill Thompson and H Bruce Stewart. *Nonlinear dynamics and chaos*. John Wiley & Sons, 2002.

[41] Peter Turchin and Ilkka Hanski. An empirically based model for latitudinal gradient in vole population dynamics. *The American Naturalist*, 149(5):842–874, 1997.

[42] Rebecca Tyson and Frithjof Lutscher. Seasonally varying predation behavior and climate shifts are predicted to affect predator-prey cycles. *The American Naturalist*, 188(5):539–553, 2016.

[43] Stephen Wiggins. *Introduction to Applied Nonlinear Dynamical Systems and Chaos*, volume 2 of *Texts in Applied Mathematics*. Springer, 2nd edition, 2003.

A. Nondimensionalization

In the following we want to nondimensionalize the summer and winter equations of our dynamics,

$$\begin{aligned}\frac{dN}{dt} &= rN\left(1-\frac{N}{K}\right)-\frac{aN^2P}{b^2+N^2}\\ \frac{dP}{dt} &= \gamma\frac{aN^2P}{b^2+N^2}+\frac{sP}{1+\nu P}-mP\end{aligned}$$

for the summer and

$$\begin{aligned}\frac{dN}{dt} &= c\,rN\left(1-\frac{N}{K}\right)-\frac{\alpha NP}{\beta N}\\ \frac{dP}{dt} &= \gamma\frac{\alpha NP}{\beta N}-\mu P\end{aligned}$$

for the winter. Like Tyson and Lutscher [42], we scale the prey population N by their carrying capacity K and the predator population by the term $\frac{rK}{a}$, which is the growth rate of the prey population divided by the predator's maximum kill rate. We write our model with dimensionless prey and predator densities $n = \frac{N}{K}$ and $p = \frac{aP}{rK}$ as well as dimensionless time $\tau = tr$.

First, start with the prey summer dynamics.

$$\begin{aligned}\frac{dn}{d\tau} &= \frac{dN}{dt}\frac{1}{Kr}\\ &= \frac{N}{K}\left(1-\frac{N}{K}\right)-\frac{1}{Kr}\frac{aN^2P}{b^2+N^2}\\ &= n(1-n)-\frac{1}{Kr}\frac{aK^2n^2\frac{rK}{a}p}{K^2\frac{b^2}{K^2}+K^2n^2}\\ &= n(1-n)-\frac{n^2p}{\left(\frac{b}{K}\right)^2+n^2}\\ &= n(1-n)-\frac{n^2p}{\tilde{b}^2+n^2}\end{aligned}$$

A. Nondimensionalization

The summer dynamics of the predator density read:

$$\begin{aligned}
\frac{dp}{d\tau} &= \frac{dP}{dt}\frac{a}{r^2K} \\
&= \frac{a}{r^2K}\left(\gamma\frac{aN^2P}{b^2+N^2} + \frac{sP}{1+\nu P} - mP\right) \\
&= \frac{a}{r^2K}\frac{\gamma aK^2n^2\frac{rK}{a}p}{K^2\left(\tilde{b}^2+n^2\right)} + \frac{a}{r^2K}\frac{s\frac{rK}{a}p}{1+\nu\frac{rK}{a}p} - \frac{a}{r^2K}m\frac{rK}{a}p \\
&= \frac{a\gamma}{r}\frac{n^2p}{\tilde{b}^2+n^2} + \frac{s}{r}\frac{p}{1+\nu\frac{rK}{a}p} - \frac{m}{r}p \\
&= \tilde{\gamma}\frac{n^2p}{\tilde{b}^2+n^2} + \tilde{s}\frac{p}{1+\tilde{\nu}p} - \tilde{m}p
\end{aligned}$$

We have introduced the dimensionless parameters $\tilde{\beta} = b/K$, $\tilde{\gamma} = a\gamma/r$, $\tilde{s} = s/r$, $\tilde{\nu} = \nu rK/a$ and $\tilde{m} = m/r$. For the winter dynamics, we proceed in the same way.

$$\begin{aligned}
\frac{dn}{d\tau} &= \frac{dN}{dt}\frac{1}{Kr} \\
&= c\frac{N}{K}\left(1-\frac{N}{K}\right) - \frac{1}{Kr}\frac{\alpha Kn\frac{rK}{a}p}{\beta+Kn} \\
&= cn(1-n) - \frac{\alpha}{a}\frac{np}{\frac{\beta}{K}+n} \\
&= cn(1-n) - \tilde{\alpha}\frac{np}{\tilde{\beta}+n}
\end{aligned}$$

$$\begin{aligned}
\frac{dp}{d\tau} &= \frac{dP}{dt}\frac{a}{r^2K} \\
&= \frac{a}{r^2K}\left(\gamma\frac{\alpha NP}{\beta N} - \mu P\right) \\
&= \frac{a}{r^2K}\frac{\gamma\alpha Kn\frac{rK}{a}p}{\beta+Kn} - \frac{a}{r^2K}\mu\frac{rK}{a}p \\
&= \gamma\frac{\alpha}{r}\frac{np}{\frac{\beta}{K}+n} - \frac{\mu}{r}p \\
&= \tilde{\gamma}\frac{\tilde{\alpha}np}{\tilde{\beta}+n} - \tilde{\mu}p
\end{aligned}$$

Again, we have introduced dimensionless parameters, namely $\tilde{\alpha} = \alpha/a$, $\tilde{\beta} = \beta/K$ and $\tilde{\mu} = \mu/r$. The addition of the winter reproduction term (compared to the seasonal equations in [42]) does not cause any problems when rescaling; the factor c just carries through the whole process and shows up in the final equation as desired.

Concluding the calculations, we collect our dimensionless seasonal model equations.

$$\begin{aligned}\frac{dn}{d\tau} &= n(1-n) - \frac{n^2 p}{\tilde{b}^2 + n^2} \\ \frac{dp}{d\tau} &= \tilde{\gamma}\frac{n^2 p}{\tilde{b}^2 + n^2} + \tilde{s}\frac{p}{1+\tilde{\nu}p} - \tilde{m}p\end{aligned}$$

$$\begin{aligned}\frac{dn}{d\tau} &= cn(1-n) - \tilde{\alpha}\frac{np}{\tilde{\beta}+n} \\ \frac{dp}{d\tau} &= \tilde{\gamma}\frac{\tilde{\alpha}np}{\tilde{\beta}+n} - \tilde{\mu}p\end{aligned}$$

For the speed rescalings using our switching function f_s,

$$f_s(\tau;\tilde{\omega},\kappa) := \frac{1}{2}\left(1 + \frac{\sin(\tilde{\omega}\tau)}{\sqrt{\sin^2(\tilde{\omega}\tau) + \kappa^2\cos^2(\tilde{\omega}\tau)}}\right)$$

we proceed as follows. As the period of f_s is $\tau = r$, we choose $\tau_0 := 0.5r$ and introduce the variable summer length as $\tau_S := rT_S$ for $T_S \in [0,1]$. We introduce the speed rescalings for summer resp. winter, as

$$\begin{aligned}a_S &= \frac{\tau_S}{\tau_0} = \frac{\tau_S}{0.5r} = 2T_S, \\ a_W &= \frac{r-\tau_S}{\tau_0} = \frac{1-T_S}{0.5} = 2(1-T_S) = 2 - a_S.\end{aligned}$$

This allows us to introduce variable summer length (via the variable $a_S = 2T_S$, $T_S \in [0,1]$), and we arrive at our final dimensionless model equations

$$\begin{aligned}\frac{dn}{d\tau} =& a_S\, f_s(\tau;\tilde{\omega},\kappa)\left[n(1-n) - \frac{n^2 p}{\tilde{b}^2+n^2}\right] \\ &+ (2-a_S)\,(1-f_s(\tau;\tilde{\omega},\kappa))\left[cn(1-n) - \tilde{\alpha}\frac{np}{\tilde{\beta}+n}\right], \\ \frac{dp}{d\tau} =& a_S\, f_s(\tau;\tilde{\omega},\kappa)\left[\tilde{\gamma}\frac{n^2 p}{\tilde{b}^2+n^2} + \tilde{s}\frac{p}{1+\tilde{\nu}p} - \tilde{m}p\right] \\ &+ (2-a_S)\,(1-f_s(\tau;\tilde{\omega},\kappa))\left[\tilde{\gamma}\frac{\tilde{\alpha}np}{\tilde{\beta}+n} - \tilde{\mu}p\right].\end{aligned}$$

B. System dynamics in limiting seasonal cases

In the following, we focus on two extreme cases of our simulation, namely when only the winter dynamics or the summer dynamics are active ($a_S = 0$ or $a_S = 2$). This allows us to investigate the impact of the single-season equations (equations (3.5) and (3.6) for summer and (3.7) and (3.8) for winter) on the dynamics of our rodent-mustelid system more clearly.

Note that the bifurcation diagram 5.1 shows that the value of the generalist predator density dependence ν has an impact on the possible dynamics for $a_S = 2$. For low ν, simulations with only summer equations active lead to a single fixed point on the Poincaré map in the long term. For higher $\nu > 3$, a quasiperiodic orbit is the sole long-term attractor.

For $a_S < 1$, the trajectories in the simulation are (at some times) very close to extinction of at least one of the species. Graphically speaking, the trajectories get close to the x- and y-axis. In a real-life scenario, this would at some point lead to extinction of the species (assuming that there is no immigration from other neighboring geographic locations). In a simulation, small values in n or p can lead to numerical errors when solving the equations. The precision and qualitative value of the simulation for $a_S = 0$ is therefore limited.

In Figure B.1, a collection of simulations is shown for the extreme cases $a_S = 0$ and $a_S = 2$ for different values of ν. In general, simulations show that increased summer lengths tend to lead to more stable predator-prey interactions, as the long-term attractors move away from the axes (and therefore away from extinction). This supports the theory that generalists stabilize ecosystems [16].

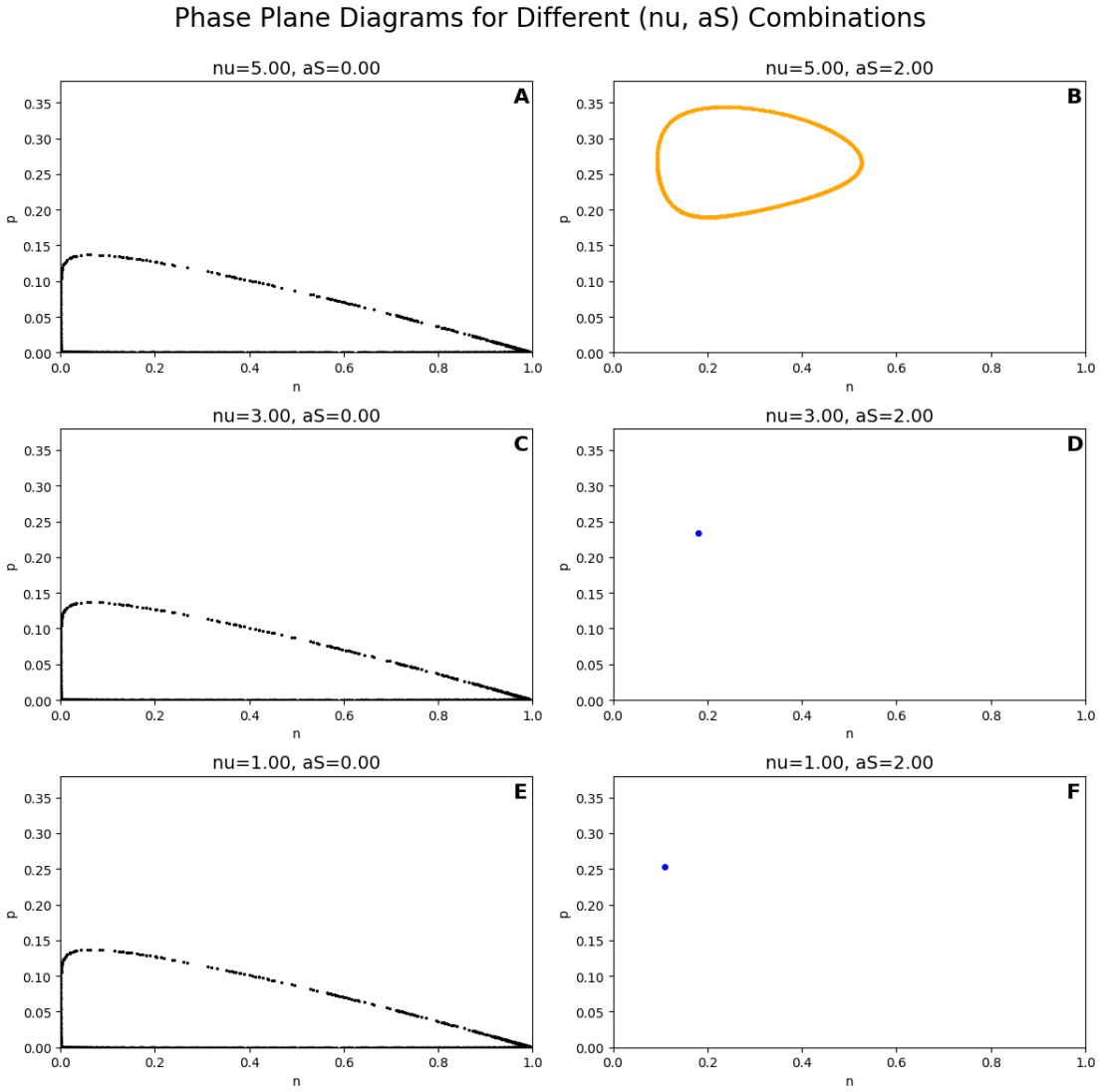

Figure B.1.: Long-term attracting structures for the extreme single-season cases, depending on the choice of parameters a_S and ν. A, C, E: Only the winter equation is active ($a_S = 0$), for $\nu = 1$ (A), $\nu = 3$ (C) and $\nu = 5$ (E). B, D, F: Only the summer equation is active ($a_S = 2$), for $\nu = 1$ (B), $\nu = 3$ (D) and $\nu = 5$ (F).

C. Combinations of various bifurcation types

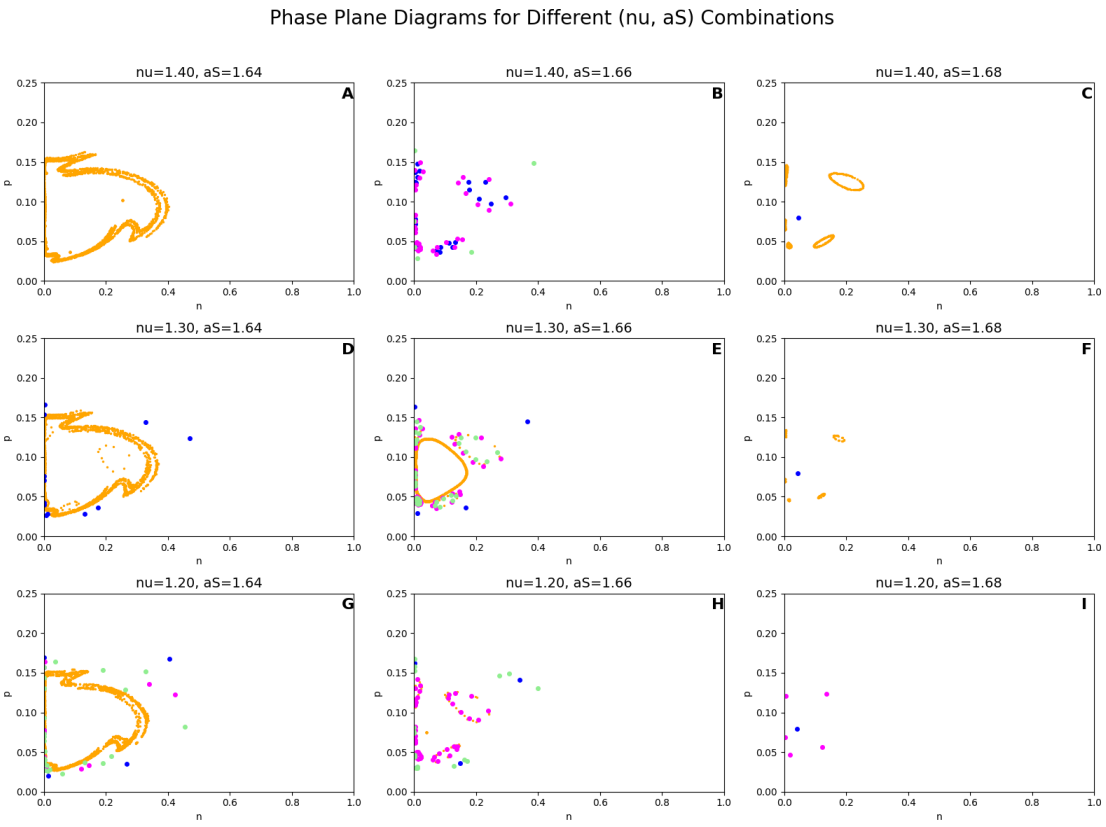

Figure C.1.: Examples for different interesting long-term attracting structures depending on the choice of parameters $\nu \in \{1.2, 1.3, 1.4\}$ and $a_S \in \{1.64, 1.66, 1.68\}$.

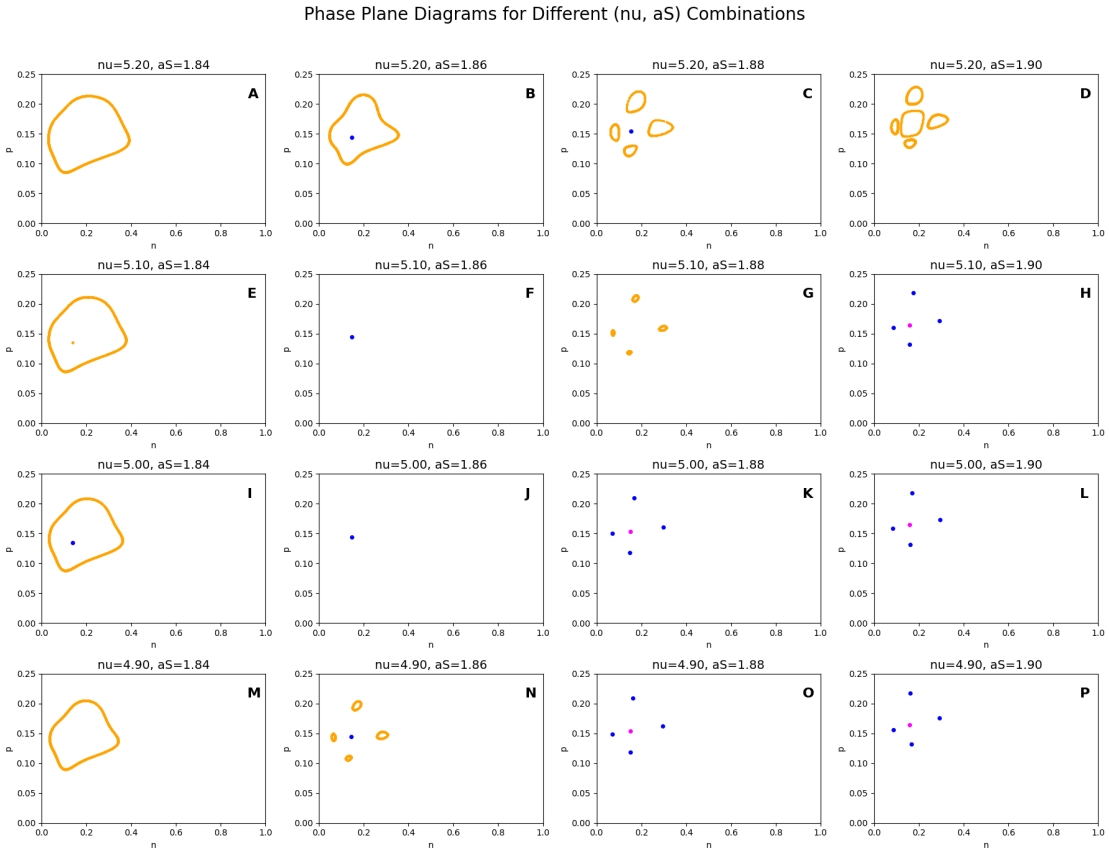

Figure C.2.: Examples for different interesting long-term attracting structures depending on the choice of parameters $\nu \in \{4.9, 5.0, 5.1, 5.2\}$ and $a_S \in \{1.84, 1.86, 1.88, 1.90\}$.

D. Fitting the exponential convergence when crossing bifurcation boundaries

Here we discuss possible reasons for the outliers of the value of k in Table 7.1, when looking at different simulations where a bifurcation boundary is crossed. k refers to the parameter for the (assumedly) linear connection between the two estimators of the speed of convergence, λ (obtained by measuring a $p \cdot 100\%$ convergence time) and κ (obtained by fitting an exponential decay via the method of least squares).

The reason for k not being approximately 1 for every single simulation lies in our approaches. If the average minimum distance curves are smooth, the estimates for the speed of convergence are very close to each other (so, $k \approx 1$). That is mostly the case where we start at a non-cyclic attractor like a quasiperiodic orbit, i.e. with many trajectories which converge to a single 1-cycle. The minimum distances are averaged over a large number of trajectories, leading to a smooth curve. Then the method of least squares gives a really good fit to the exponential decay (see Figure D.1 for example - this corresponds to simulation 11 in Table 7.1, where $k = 1.08$).

Furthermore, also the other estimator gives a good fit, as in contrast to when the data for the exponential decay are not always monotone decreasing (see Figure 7.2 for example, where there seem to be periodic fluctuations in the generally exponentially decreasing curve), the smooth curve allows for a reliable estimator of t_p and thus a good approximate exponential decay function. (See Remark 7.1.1 as well)

If the average minimum distance curves are not smooth (for example, if there are only few trajectories, thus the average minimum distance is still susceptible to outliers), or the exact location of the attractor is not fully known, but only at some numerical approximation (that is, for chaos - see Remark 7.2.1), both approaches lead to slightly different approximations.

In general, the speed of convergence approach tends to overestimate the speed of convergence, as it uses the very first time for which the data lie below $p \cdot 100\%$ of the initial value (even if the curve then increases again), leading to a faster exponential decay. The least-squares approach tends to underestimate the speed of convergence, as in the first few years the decay is often not yet exponential.

Very low values of k in Table 7.1 correspond to simulations starting at a 1-cycle and converging to a quasiperiodic orbit (for simulation 6 - $k = 0.392$) or chaos (for simulation

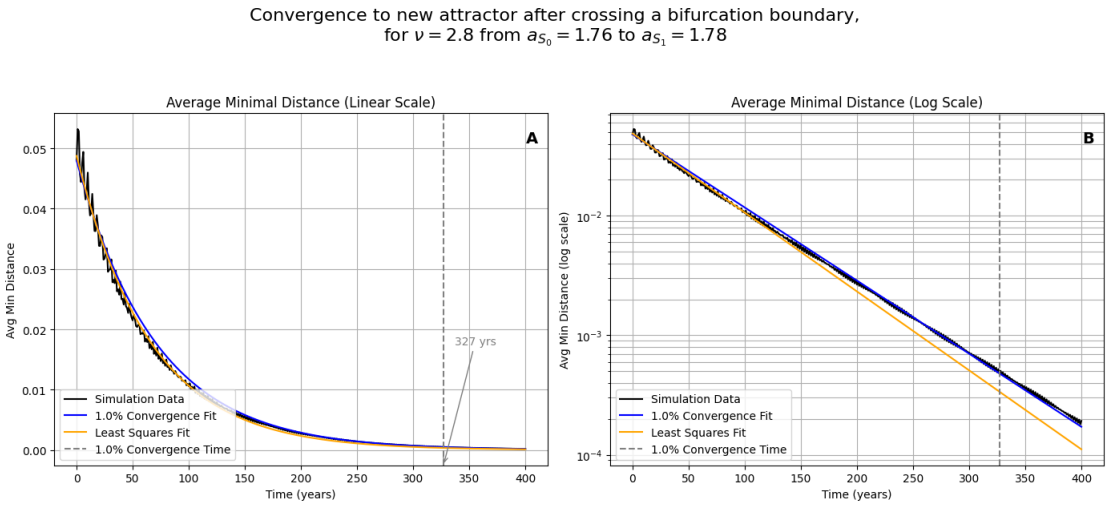

Figure D.1.: Smooth average minimal distance to attracting structure after crossing a boundary, for $\nu = 2.8$ from $a_{S_0} = 1.76$ (quasiperiodic orbit) to $a_{S_1} = 1.78$ (1-cycle). The average minimal distance is plotted in black. The estimated exponential decay functions are plotted in blue (fitted via the 1% convergence time) resp. orange (fitted via least-squares). A: simulated data and the estimators for exponential decay in linear scale. The 1% convergence time is $t_{0.01} = 327$ years. B: simulated data and the estimators for exponential decay in logarithmic scale.

9 - $k = 0.204$). The initial point (1-cycle) lies very close to some of the locations of the attractor, but very far away from others (as the chaotic orbits span to high values of prey density n). Therefore, as the trajectory converges to the chaotic attractor, at some times it will be close to the attractor and at some times still far away - leading to not only slow convergence, but also high fluctuation in the minimal distance (even more so, as there is only one initial condition and so outliers cannot be accounted for by averaging). Supported by this fluctuation, the two estimators give very different approximations for the speed of convergence, see Figure D.2.

In Figure D.2 one can also see the impact of not knowing the exact locations of the full chaotic attractor. For large time t, one can see recurring spikes in the average minimal distance, whereas in general the system seems to have converged already. Because not all locations of the attractor are known, those outliers correspond to an area, where the nearest point in our numerically obtained chaotic orbit is $\varepsilon \in [0.002, 0.015]$ away[1]. Letting the simulations run longer and, therefore, obtaining more points in the Poincaré map

[1] In the left plot in Figure D.2, we see that for late times, the average minimum distance keeps jumping to values around 0.01. This means, that the nearest numerically obtained point in the attracting chaotic orbit is at least this much away, thus ε needs to be bigger than the maximum of all of them, thus its value probably lies within $[0.002, 0.015]$.

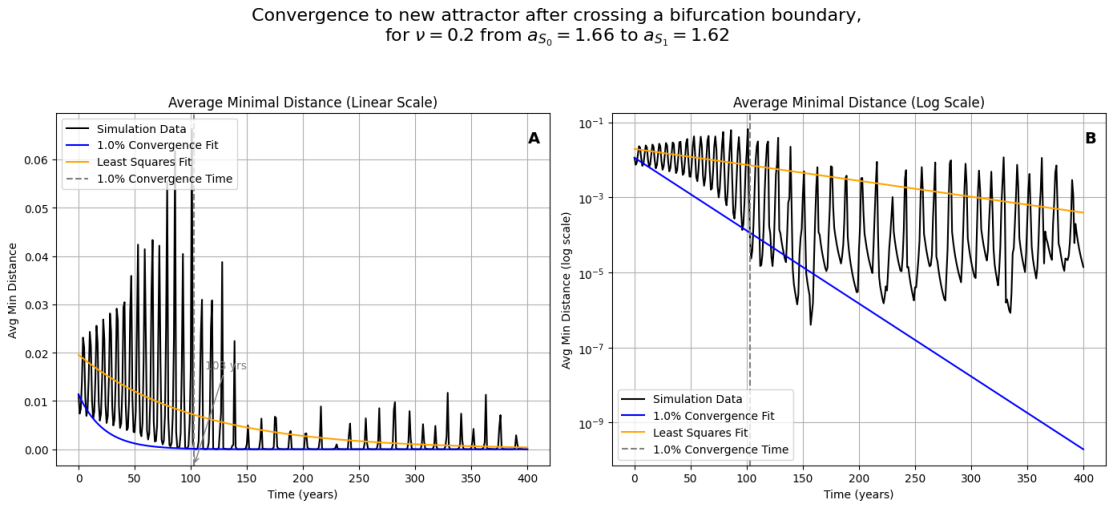

Figure D.2.: Large fluctuations in average minimal distance to attracting structure after crossing a boundary, for $\nu = 0.2$ from $a_{S_0} = 1.66$ (1-cycle) to $a_{S_1} = 1.62$ (chaos). The average minimal distance is plotted in black. The estimated exponential decay functions are plotted in blue (fitted via the 1% convergence time) resp. orange (fitted via least-squares). A: simulated data and the estimators for exponential decay in linear scale. The 1% convergence time is $t_{0.01} = 104$ years. B: simulated data and the estimators for exponential decay in logarithmic scale.

for the chaotic orbit, would decrease these numerical errors. However, the fluctuations in the beginning (for the first 150 years) would likely still persist in the system.

Figure D.3 shows the case for which the initial average minimum distance is already very small and those numerical errors are too big to find an estimator via the 1% convergence time. In such cases, one can use equation (7.6) and the estimator for the speed of convergence from the least-squares method κ to arrive at a reasonable approximation of the 1% convergence time $t_{0.01}$.

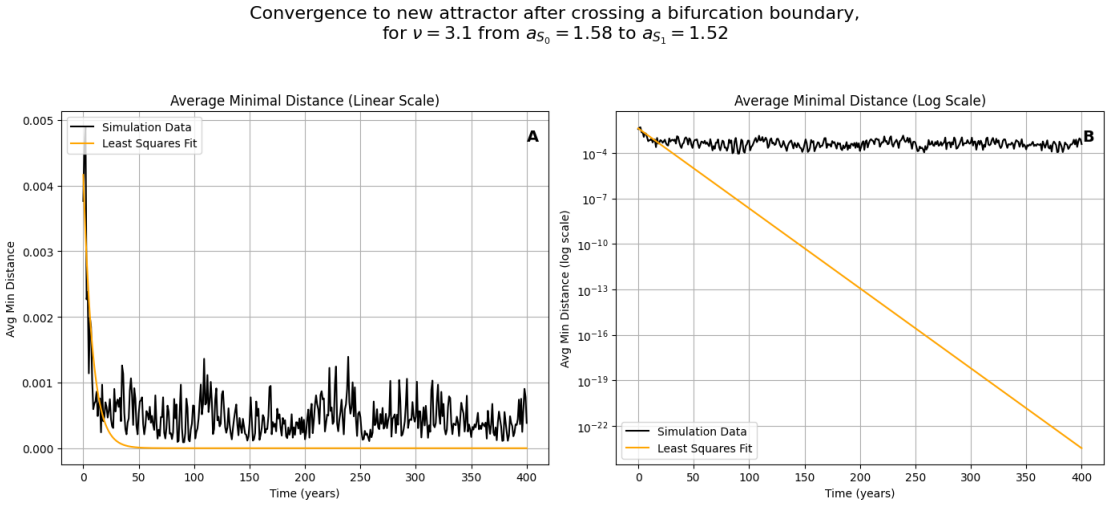

Figure D.3.: Average minimal distance to attracting structure after crossing a boundary, for $\nu = 3.1$ from $a_{S_0} = 1.58$ (20-cycle) to $a_{S_1} = 1.52$ (chaos). The average minimal distance is plotted in black. Not both approaches to find an exponential decay function were successful. There is no fit via the 1% convergence time. The fit by the least-squares method is plotted in orange. A: simulated data and the estimator for exponential decay in linear scale. B: simulated data and the estimator for exponential decay in logarithmic scale.

List of figures

List of tables